Probing Multiscale Structure of Mineral and Nanoporous Kerogen Phase in Organic-Rich Source and Neutron Scattering

Gaël J Cherfallot, Pierre E Levitz, Pauline Michel, Eric Kohler, Jacques Jestin, Loïc Barré

Probing Multiscale Structure of Mineral and Nanoporous Kerogen Phase in Organic-Rich Source Rocks : Quantitative comparison of Small-Angle X-ray and Neutron Scattering

Gaël J. Cherfallot[†‡*], *Pierre E. Levitz*[†], *Pauline Michel*[‡], *Eric Kohler*[‡], *Jacques Jestin* [] *and Loïc Barré*[‡*]

[†]Sorbonne Université, CNRS, UMR 8234, Physicochimie des Electrolytes et Nanosystèmes Interfaciaux, 4 place Jussieu, F-75252 Paris, France

[‡]IFP Energies Nouvelles, 1 et 4 avenue du Bois-Préau, 92852 Rueil-Malmaison, France

[]Laboratoire Léon Brillouin, UMR 12, CEA Saclay, 91191 Gif-sur-Yvette cedex, France

* Corresponding authors – Email gael.cherfallot@ifpen.fr , loic.barre@ifpen.fr

ABSTRACT

Source rocks are expected to become increasingly important in the upcoming years for oil and gas production as well as for the storage of greenhouse gases. These rocks are bedded and heterogeneous media, composed of minerals, kerogen and pore space. One of the most challenging issue is to better

define the pore space, including pore size distribution, pore volume fraction, pore connectivity and pore affinity for various fluids. The aim of this study is to achieve such relevant parameters using X-ray and neutron scattering techniques complementarity. Rocks thin blades cut normal to bedding plane preserve sample integrity and allow their measurements on both techniques. 2D scattering patterns show anisotropy, due to preferential orientation of lamellar minerals, which allows us to assess an order parameter. This parameter is a valuable tool for mechanical and transport properties. A model based on a three-phase system (minerals, kerogen and pores) is developed through the study of scattering length density of each component within both radiations. The model allows us to fit both X-ray and neutrons 1D data using the same model parameters. This later is then considered as selective. It allows us to extract the kerogen mass density, the kerogen pore size distribution and its associated volume fraction, and the chemical nature of kerogen pore content. This methodology has been applied to a series of five source rocks of increasing maturities, from Barnett Shale Play and Montney-Doig formations. Mature samples show a kerogen density of ~1.6 $g.cm^{-3}$, a pore radius distribution centered on 0.5 – 0.7 nm accounting for a pore volume fraction of ~ 0.01-0.04. These kerogen nanopores are filled by light condensed hydrocarbons. However, the overmature kerogen exhibit a mass density of 1.74 $g.cm^{-3}$, an additional pore radius distribution centered around 3.5 nm with a pore volume fraction of 0.002 and an empty pore space. All these parameters are in agreement with Rock-Eval pyrolysiss measurements and literature data on similar source rocks. These results pointed out that the three-phase model associated with X-ray and neutron complementarity could be applied to *in-situ* studies.

1. INTRODUCTION

Source rocks formations are one of the most widespread reservoir on earth[1] and display a high potential of storage capacity.[2] Since recent years, gas and oil coming from organic-rich source rocks systems, also known as shale gas, present an increasing interest in North American and Asian

countries.[3-4] In the next decade, shale gas production will reach almost a fifth of the world natural gas production.[4] Thus, such geological system is expected to be intensively exploited in the upcoming years.[5] The source rocks are reported in the literature as a heterogeneous[6] and anisotropic media[7-10]. Shale gas are complex systems composed of several types of minerals (*i.e.* silicates, phyllosilicates, tectosilicates, carbonates and iron sulfide) combined with organic matter (*i.e.* kerogen, bitumen and pyrobitumen).[11] The rock anisotropy observed within bedding structures suggests that a preferential orientation condition the fluid flows through the system.[12] The porous media are contained by both, organic or inorganic phases with macropores (> 50nm) and mesopores (from 50nm to 2nm) mainly located in minerals, and micropores (< 2nm)[13] mostly encountered in the organic phases[14-15] or in the interlayer space of clay minerals. Fluids in pore space, such as gas and oil, are released by the organic phase during the burial process.[16] As it is also well known, this material has a low permeability (in the range of nD),[17] low porosity and high retention capacity through physisorption mechanism[18-19] which may vary depending on the rocks micropores content. Currently, a scientific interest on source rocks transport and storage properties led to an investigation on rock porosity.[8,20-25] Studies are focusing on the improvement of nanoporous media understanding through the assessment of total porosity,[23,26-32] open versus closed pores content,[10,33] pore size distribution,[10,14,15,17,20-23,27,28,34-39] their connectivity[8,10,21,28,34] and the porous network tortuosity.[34,40] Accordingly, several analytical methods are employed such as gas adsorption/desorption,[23,27-30,41] mercury injection capillary pressure,[17,21,25,28,36,42] NMR relaxometry,[43,44,45] NMR cryoporosimetry,[46] multifrequency and multidimensional NMR[47] and Small-Angle Neutron Scattering (SANS).[6,15,20,23,27,28,34,35,39,48]

SANS is used to bring details on the source rocks total porosity[28,38] and to determine their pore size distribution (PSD).[10,23,28,38] A dedicated workflow was developed from a few decades through the acquisition of SANS data.[6,15,20,23,27,28,34,35,39,48] Classically, source rocks are described as a two-phase

system, depending on the matrix (*i.e.* mineral and organic matter) and the pore space. Then, scattering data are modeled by the polydisperse spherical pore (PDSP) model weighted by a term of contrast between the sample matrix and the pores space.[20,27,28,34,35]

The model describes the scattering intensity *I(Q)* of diluted spherical pores of radius *R* (Equation 1) as a function of the volume fraction, $\phi = \int_{Rmin}^{Rmax} N(R).V(R)\ d(R)$, of polydisperse spheres, the form factor *P(Q,R)* of spheres, and their volume, *V(R)*. Such model depend on the squared Scattering Length Density (SLD) ρ difference of the considered phases, such as the matrix or the pore space, and can be expressed as follows:

$$\boldsymbol{I(Q) = \left(\rho_{matrix} - \rho_{pores}\right)^2 \int_{R_{min}}^{R_{max}} N(R).V^2(R).P(Q,R)\, d(R)} \tag{1}$$

From these modeling a PSD is determined as well as the sample total porosity ϕ. Small-angle scattering is one of the rare technique which probe the total pore space. Both SAXS and SANS techniques, are based on the same principle, it is then possible in theory to obtain similar results[48]. However, small-angle X-ray scattering on source rocks is less investigated[49,50] than SANS owing to the presence of pyrite, with a different SLD than other minerals, introducing a supplementary phase. Beam types as neutron or X-ray have a different interaction through the material which can be exploited as a complementary. Indeed, the different X-ray and neutron contrast are expected to better define the chemical nature of fluids in pore space.

Herein, this work is focused on the neutron and X-ray scattering profiles similarities and complementarities. The aim is first to provide details on the minerals orientation, the kerogen mass density, pore size contained in the kerogen phase and their associated volume fraction, and then to assess the nature (gas or oil) of fluids in place. A multi-technical approach through the comparison of

X-Ray diffraction, Rock-Eval pyrolysis, Headspace gas chromatography, Field-Emission Scanning Electron Microscopy and small-angle scattering techniques, is expected to bring rocks structural information. For that, five source rock samples are selected based on their petrological and geochemical properties to form a continuous sequence of organic matter maturity. Their X-ray and neutron scattering intensities are then compared in order to get new information on (i) minerals orientation relatively to the bedding plane, (ii) the maturity of kerogen, (iii) the pore size distribution and the occupancy of pores in respect to gas or hydrocarbon phase.

2. MATERIALS AND METHODS

2.1. Source rocks.

Source rocks chosen and used in this study were provided by IFPEN and were collected from two geological North-American Formations as part of research projects dedicated to unconventional oil and gas reservoirs (GASH European program (2009-2012) and MGH IFPEN internal research program). Four samples named as BSP-2, BSP-3, BSP-4 and BSP-5 come from the Mesquite 1 well of the Barnett Shale Play (BSP) (Texas – United States). The BSP samples were deposited in a foreland basin in the Fort Worth Basin. These rocks are fine grained laminar silicate-rich and organic-rich source rocks. The last sample MT-1 originates from the Cypress field (well C-30-l / 94-b-15) of the Montney-Doig Formation (MT) (Alberta and British Columbia – Canada). This sample was deposited during sediment accumulations in a foreland basin. It is a laminated coarse grained silicate-rich and organic-rich rocks. In the *Table 1*, general information about the sample geological formation and the depth at which they were collected, are listed.

105 **2.2. Sample preparation.**

106 For Rock-Eval pyrolysis and X-Ray Diffraction (XRD) measurements, samples were crushed into <
107 50 µm powders. HeadSpace Gas Chromatography (HS-GC) analysis was performed on rock sections
108 cut parallel and also cut normal to bedding. These sections were shaped into parallelepiped subsample
109 of about 1 x 2 x 0.2 cm. Field Emission Scanning Electron Microscopy (FESEM) observations and
110 scattering measurements were made on rock thin blade sections cut normal to bedding. A schematic
111 summary for sample preparation according to the technique used is illustrated *Figure 1*.

112 Source rocks are a heterogeneous systems where a representative volume is difficult to assess. In
113 addition, the comparison between Small-Angle Neutron Scattering (SANS) and Small-Angle X-ray
114 Scattering (SAXS) measurements requires to be performed on a similar probed volume as both
115 techniques have different beam sizes, classically 0.5 x 0.5 mm for SAXS and 5 x 5 mm for SANS.
116 Sample thickness optimization is also important as optical path is related both to the sample
117 transmission, different for each radiation, and to multi scattering issues.[22,33,35,38,39,51] In the chosen
118 conditions (see below), transmission is high for SANS about 90 %, and low for SAXS, around 10 %.

119 From these considerations and prior to this study, the sample thickness and the probed volume
120 homogeneity were assessed on a sample, called MT-2, with a low Total Organic Carbon (TOC)
121 content (1.4 %wt), extracted from the well 0/14-32-073-08W6 of the Montney-Doig formation at a
122 depth of 2070 meters. This well is located at 270 Km South-East of MT-1 sample. MT-2 was chosen
123 to evaluate the effect of mineral variability on scattering intensity, as it have a low TOC content. The
124 influence of sample thickness on SAXS data were analyzed to determine the occurrence of multiple
125 scattering effects. SAXS measurements were conducted on MT-2 normal cut to bedding thin blade
126 sections within a thickness of 100, 140 and 210 µm. Scattering intensities were normalized to the
127 sample thickness and transmission. Results (supplementary information) show that intensities in

absolute units are about the same according to three different sample thickness suggesting (i) no multiple scattering in this Q range and (ii) measurements are performed in an almost homogeneous probed volume. The multiple scattering effect was only checked on SAXS data assuming, as suggested by Anovitz and Cole (2015), the fact that if the transmission is greater than 90 %, the multiple scattering effects remains small.

To complete our view on probed volume homogeneity, SAXS measurements were performed on 9 and 5 random positions on the 140 µm thick MT-2 sample with a 200 x 200 µm beam size. Results were decomposed as the sum of power law trends as $A.Q^{-\alpha}$. Then, the A or α parameters were used to define the variability of each parameter. The α parameter vary within 1% whereas the prefactor vary within less than five percent. The latter is thought to be correlated with concentration, size and contrast of various scatterers. We conclude from the low dispersion of A and α parameters that with this beam size, the sample phase distribution is almost constant. Moreover, the SAXS intensities measured on 9 or 5 random positions were averaged to get a more representative volume to be compared with neutron measurements.

As this study is partly focused on the analysis of source rock anisotropy, the samples were cut normal to bedding plane to maximize the occurrence of lamination, as shown in *Figure 1*. Rocks thin blade sections with a maximum thickness of 200 µm were prepared and stuck to pierced quartz blades with a pinhole of 5.5 mm diameter. This diameter allows to map and to average several SAXS measurements in order to probe about the same volume as SANS ; in this way, the comparison of X-ray and neutron scattering intensities are meaningful. Concerning the homogeneous probed volume of samples used in this study, SAXS measurements were performed on five random location for each sample. Obtained scattering intensities were checked and compared to the mean intensity. It reveals no

150 significant variation allowing us to consider that the probed volume display a constant phase
151 distribution.

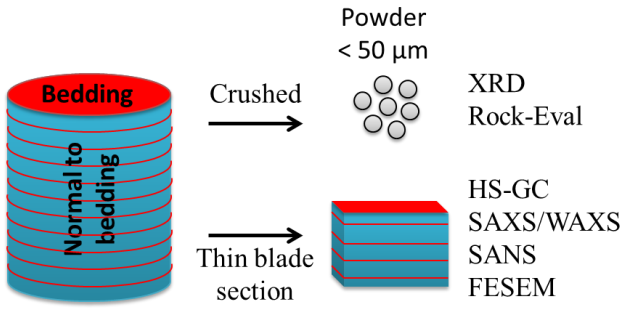

152 ***Figure 1.*** *Schematic representation of sample preparation with in blue normal to bedding plane and*
153 *in red the bedding.*

154
155
156 **2.3. Rock-Eval® 6 pyrolysis.**
157
158 Geochemical data on organic matter were obtained by Rock-Eval pyrolysis according to the Shale
159 Play method.[31,52] This technique is used to define the TOC content, the organic matter type and the
160 maturity through HI vs Tmax diagram, as shown in *Table 1* and in *Figure 2*.[11,23,24,26,28-31,34,35,53-55]
161 Analysis was performed on 60 mg of dry bulk-rock powder and standard deviation was assessed
162 through the repeatability of five measurements of each sample.
163 Samples have a TOC content ranging from 4.5 %wt (BSP-2 and BSP-3) up to 9.0 %wt (BSP-4). The
164 *Figure 2* illustrates sample measurements, all of them are consistent with a kerogen of type II.[56,57]
165 These samples follow an increasing depositional depth from BSP-2 (1126 m) to MT-1 (2561 m). BSP
166 samples are mature, as HI range from 146 to 174 mg HC / g TOC and Tmax is close to 445°C. They
167 are in the oil window and the MT-1 sample reach the dry gas window which means that it is
168 overmature (HI = 17 mg HC / g TOC and Tmax = 598°C). As shown by Craddock and coworkers

169 (2018),[11] there is a strong correlation between the depositional depth and the maturity of the sample.

170 An increase of the maturity along the depth is then expected.

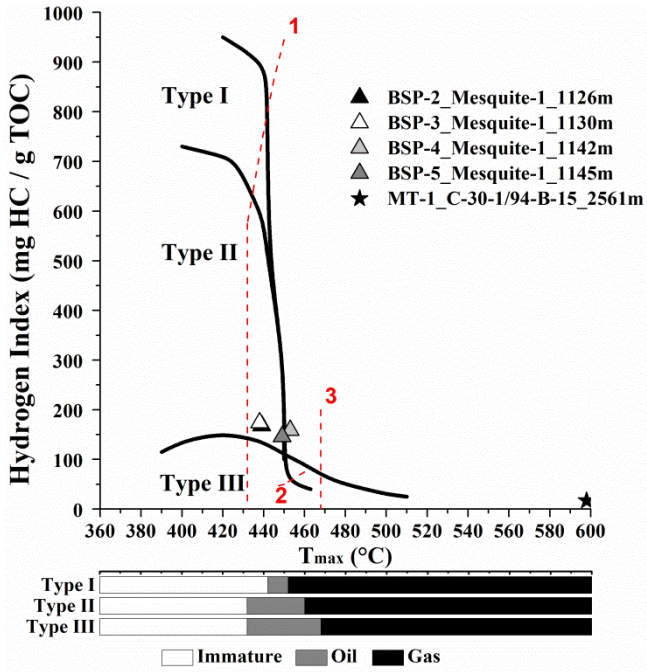

171 ***Figure 2.*** *HI as a function of Tmax diagram with delineations 1, 2 and 3 defining the limit of the oil-*

172 *gas window for kerogen of type I, II and III.*[54] *BSP samples are represented by triangles and MT-1 is*

173 *symbolized by a star.*

174 ***Table 1.*** *Rock-Eval pyrolysis data obtained within the Shale Play method on the five source rock*

175 *samples. (a) Data expressed in mg HC / g rock.*

Formation	Reference	Well	Depth m	Maturity	Sh0 (a)	Sh1 (a)	Sh2 (a)	Tmax (°C)	HI mg HC / g TOC	TOC wt %
Barnett Shale Play	BSP-2	Mesquite 1	1126.7	Mature	2.36	2.7	7.5	439	168	4.5
	BSP-3	Mesquite 1	1130.5	Mature	2.55	3.5	7.8	438	174	4.5
	BSP-4	Mesquite 1	1142.4	Mature	2.09	3.0	14.5	453	159	9.0
	BSP-5	Mesquite 1	1145.4	Mature	1.57	2.5	11.9	449	146	8.1

Montney-Doig	MT-1	C-30-1 / 94-b-15	2561.8	Overmature	0.09	0.3	0.8	598	17	4.8
	Standard deviation				±0.06	±0.02	±0.04	±0.6	±0.6	±0.01

176 **2.4. HeadSpace Gas Chromatography.**

177 To obtain detailed information on Sh0 peak and on the free hydrocarbon composition, samples are
178 characterized by HS-GC. This thermodesorption method is based on a partial pressure equilibrium
179 between the fluid in the source rocks and the vapor outside the rock generated at a given temperature.
180 For that purpose, this technique is only used as qualitative tool in this study on thin rock section
181 samples whom preparations and representations are described in section 2.2. HS-GC measurements
182 were performed on an Agilent 7890B-GC chromatograph equipped with a Headspace Sampler Agilent
183 7697A. Samples were put into a 15mL vial at 80°C between 5 minutes to 7 days. Then, a volume of
184 15 µL is taken from the vapor and injected into the chromatograph. Data on the composition between
185 C_1 and C_{11} were acquired using a chromatographic column consisting in a fused-silica capillary coated
186 with Al_2O_3 of about 30 meters with a flow rate of $1.6.10^{-2}$ $mL.s^{-1}$, an input temperature of 160°C and
187 output temperature of 210°C. Data were normalized to the sample weight and compared to a standard
188 (Supelco© n°21823895) for the peak indexation.

189 The distribution of *n*-alkane obtained by HS-GC as a function of heating time and retention time is
190 represented in *Figure 3* for the BSP-4 sample cut normal to bedding plan. Based on this sample study,
191 light compounds such as C_1 to C_8 are shown to be preserved during the sample preparation. Results
192 from chromatographs reveal that, at t = 4 min to 10 min, the main contribution to hydrocarbon
193 composition are ascribed to light compounds from C_1 to C_5. Over several heating times, from 5
194 minutes to 7 days, the gas distribution remains unchanged with an increasing pressure. This reveals an

uncompleted gas release as no partial pressure equilibrium between the vapor outside and the fluid in the rock is reached. One may explain it by the rock composition which contains silicates with Si-OH groups and also illite and feldspar with Al_2O_3 groups which act as retention sites. Such functional groups are classically used in chromatographic fused-silica column as adsorption surfaces. Thus, a chromatographic effect can be observed in the rock as adsorption/desorption can occur on functional groups leading to an uncomplete desorption within the heating time used. Anyway, this suggests that the diffusion through the sample is low which is consistent with a low permeability as source rocks porous media display connected and disconnected pore spaces.[7,27,34,55,58-61] Measurements on parallel and normal cut to bedding plane were also performed, for heating times ranging from 5 to 480 minutes. Results, shown in supplementary information, reveal that desorption rate, at a given time, is always lower for parallel cuts to bedding plane than for normal ones.

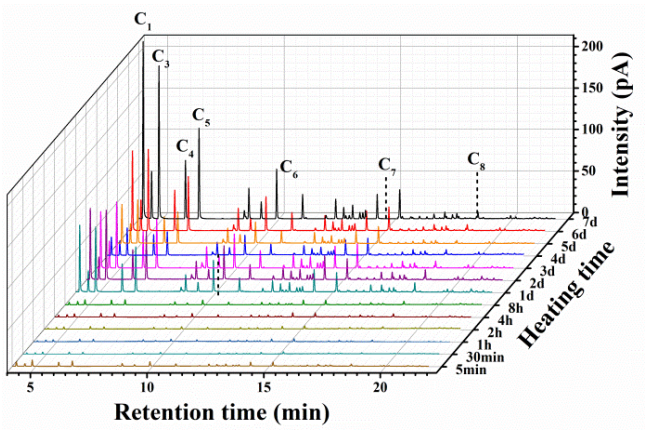

Figure 3. *Chromatographs of the BSP-4 sample, cut normal to bedding plan, over several heating times, from 5 minutes to 7 days, in an oven at 80°C.*

2.5. XRD Measurements.

The mineral composition was determined using a PANalytical X'pert Pro diffractometer using a detector X'celerator and equipped with a Copper X-ray tube (Cu-Kα = 1.5418 Å). Data were acquired on disoriented powder samples and according to the following analytical conditions: 45 kV, 40 mA,

212 angular sector from 2 to 80 °2θ. Then, minerals quantification in weight percent, was achieved by
213 Rietveld[62] analysis using the software X'pert High Score Plus.

214 The mineralogical composition of the five studied source rocks is given in *Table 2*. The mineral
215 content in weight percent, is then converted in volume percent for the SLD calculation. The major
216 mineral phase encountered in BSP and MT samples are silicates *lato sensu* with quartz as main
217 mineral (> 30 vol %) followed by illite (4 to 20 vol %) and muscovite (15 to 28 vol%). The second
218 contribution to mineral phase is carbonate minerals with 4 to 27 vol %. Then, pyrite content varies
219 from almost 1 vol % to 2.5 vol %. This mineral composition agrees with other studies on the same
220 geological formations.[56,63]

221

222 ***Table 2.*** *Normalized mineral compositions of BSP and MT samples converted in volume percent (vol*
223 *%) using the mineral density (a) defined in the database www.webmineral.com.*

Phase	Density (g/cm^3)	BSP-2 (vol %)	BSP-3 (vol %)	BSP-4 (vol %)	BSP-5 (vol %)	MT-1 (vol %)
Quartz	2.65[(a)]	41.9	41.7	30.1	31.6	36.4
Albite	2.62[(a)]	12.0	9.0	15.4	12.5	6.5
Muscovite	2.90[(a)]	15.6	13.7	28.0	22.5	17.9
Illite	2.75[(a)]	12.4	14.8	19.8	12.8	4.1
Calcite	2.71[(a)]	8.5	12.7	-	17.4	8.6
Dolomite	2.87[(a)]	8.5	7.1	-	1.4	18.3
Apatite	3.19[(a)]	-	-	4.3	-	-
Pyrite	4.93[(a)]	1.1	0.9	2.3	1.8	2.5

224

225 **2.6. Field-Emission Scanning Electron Microscopy.**

Visual information on phase distribution is required to determine the occurrence of scattering contrast. For this reason, FESEM was used in order to acquire images on rock structures and organo-mineral phases distribution at a large scale (from hundreds of microns to dozens of nanometers). Observations on normal cut to bedding plane samples were made at 12 nm/pxl. Experiments were carried out on a FESEM Nova NanoSEM 450 on cryogenic argon ion polished sample. Images were acquired with a working distance ranging from 5.2 to 5.5 mm and a probe current of 2.5 KV.

The FESEM images of rock structures and phase distributions are shown in *Figure 4*. Four Fields of View (FOV), from 51 µm down to 2,5 µm, were observed to account for the orientation of micas and clay minerals, the pores in mineral matrix and the pore within the kerogen phase. Five types of structure are identified:

- Pyrite, crystallizing in a cubic system as framboidal and cubic shapes, have a high absorption coefficient leading to white objects on FESEM images,
- Dark grey aggregates account for the organic matter as this material is composed of light elements with a low absorption coefficient,
- Dark grey level is assigned to pores in both organic and inorganic phases,
- Subangular minerals, with a light grey level between the organic matter and pyrite minerals, are attributed to quartz,
- Feldspars, with the same grey level as quartz, exhibits an angular shape allowing their identifications,
- Carbonaceous minerals, similar to feldspars in shape, have a higher density. These minerals have also an angular shape but some intra-granular pores can be encountered owing to liquid dissolution phenomenon which is used for the identification,
- Macroscopic elongated minerals, larger than two microns, are micas,

- Fine elongated minerals, lower than two microns, are consistent with clayey mineral such as illite.

Figure 4(a), Figure 4(b) and *Figure 4(c)* display macroscopic observations (FOV = 51 µm and 13 µm) on the BSP-4 (a and b) and BSP-5 (c) samples depicting a preferential orientation of micas and clay minerals. Such features exist at a lower scale (FOV = 2,5 µm) as well as in *Figure 4(d)* coming from BSP-5 sample. Moreover, *Figure 4(c)* highlights that isolated porosity exists in the minerals and is mostly widespread in carbonaceous phases. Comparing *Figure 4(c)* and *Figure 4(d)*, shows that pores in minerals are mainly macropores with a lower amount of mesoporosity while mesopores are the major porosity in organic matter.

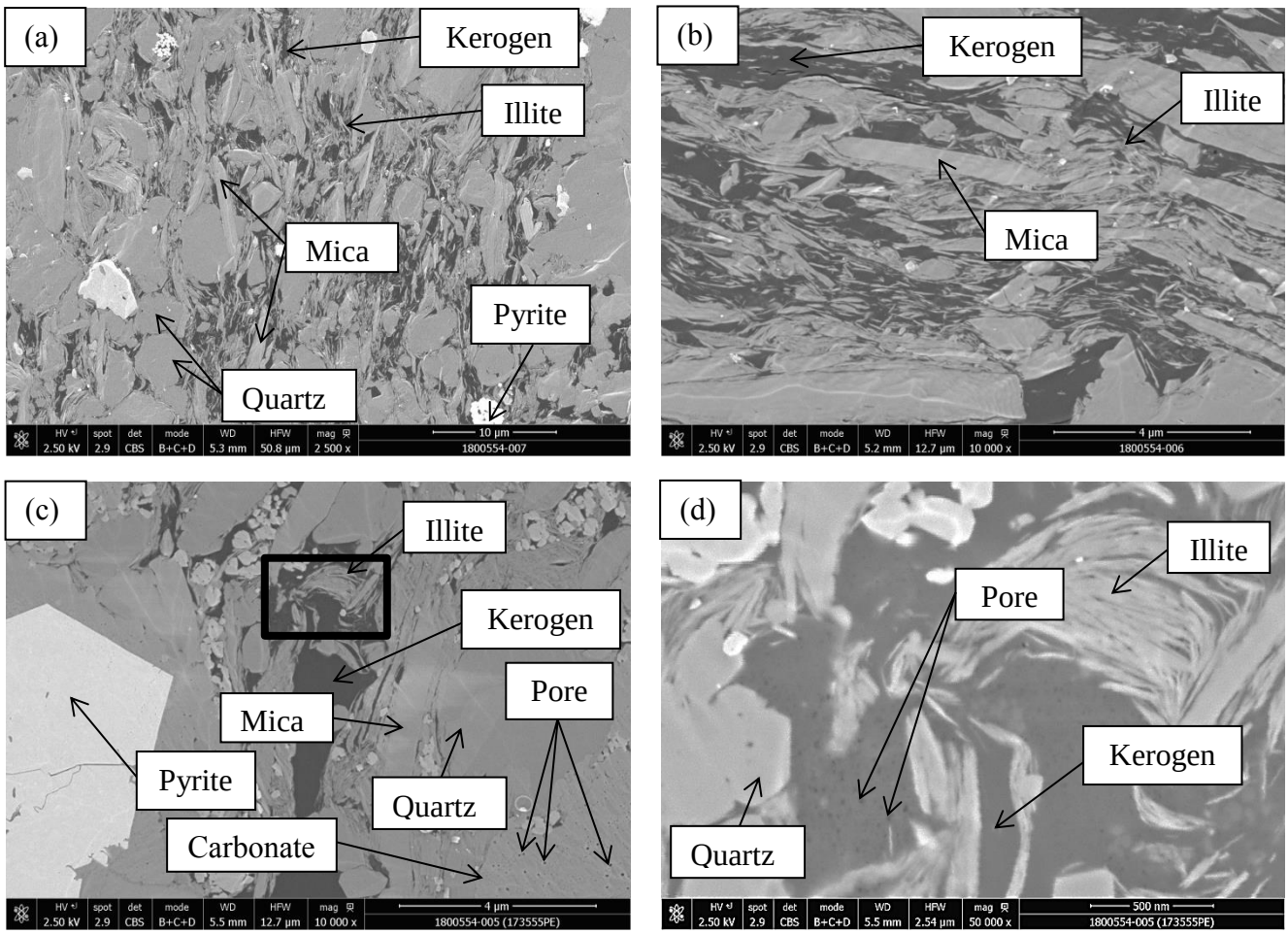

Figure 4. *FESEM observations performed on BSP-4 (a and b) and BSP-5 sample (c and d) with different fields of view, (a) 51 µm, (b) and (c) 13 µm and (d) 2,5 µm, to depict the phase distribution. The delimited area in (c) represented the field of view observed in (d).*

2.7. Scattering experiments

2.7.1. SAXS and WAXS measurements. SAXS instrument is equipped with a Cu rotating anode (Rigaku MM07, at the wavelength of $\lambda = 1.5418$ Å) and a 2D detector (Rigaku). The sample to detector distance is about 73.6 cm and allows the measurement of a scattering vector Q ranging from 0.03 $Å^{-1}$ up to 0.6 $Å^{-1}$. The instrument is also equipped with a WAXS 2D detector and enlarges the studied area until 1.6 $Å^{-1}$. The experimental setup is illustrated *Figure 5*. The scattering vector Q can be seen as an inverse correlated length scale in the reciprocal space and is defined as $Q = 4\pi.sin\theta/\lambda$ with 2θ being the scattering angle. In the case of source rocks, WAXS measurements allows the identification of the 001 Bragg peaks of illite located at $d_{001} = 2\pi/Q = 10.0$ Å. SAXS/WAXS data of each sample were corrected to their transmission, their thickness, the empty beam signal and normalized to a lupolen standard. The scattering intensity obtained on WAXS data are rescaled to the scattering intensity of SAXS data. Thus, the scattering intensity is expressed in absolute unit, cm^{-1}, for both techniques. The presence of a continuous and flat background on WAXS data at high Q values indicates the occurrence of a signal distributed over 4π which doesn't depend on Q vector. Two phenomena can contribute to the background at high Q values : (i) mineral in homogeneities at sub nanometer length scale giving rise to scattering intensities with small Q dependence , and (ii) fluorescence, since the *Cu-Kα* energy (8.04 KeV) and *Fe K*-edge energy (7.11 KeV) are close and lead to a constant scattering, independent of the Q vector. As WAXS data allow to observe a very constant background over high Q values, this phenomenon is attributed to the fluorescence of the iron contained in pyrite which needs to be subtracted, as shown in *Figure 6(a)*.

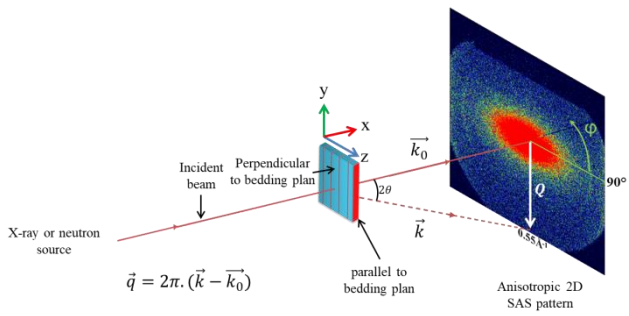

Figure 5. *Schematic representation of SAXS/WAXS configuration with respect to the laboratory frame (x,y,z).*

2.7.2. SANS measurements. SANS experiments were carried out on the PA20 spectrometer at Laboratoire Léon Brillouin (CEA/CNRS) at Saclay, France. Three different configurations ((i) λ = 3.8 Å/sample-to-detector distance (D) = 1.1 m, (ii) λ = 6 Å/D = 8 m and (iii) λ = 15 Å/D = 17.5 m), gives a total Q-range from $9.1.10^{-4}$ Å^{-1} to $5.1.10^{-1}$ Å^{-1}. To be compared with SAXS/WAXS data, it is mandatory to express the SANS intensity in absolute units. For that purpose, SANS measurements of each sample were also corrected by their transmission, their thickness, the detector pixel efficiency and normalized to the incident beam. Assuming that the almost flat background at high Q values is related to the incoherent scattering of the hydrogen contained in the sample, the mean intensity value of the last Q values (0.45 to 0.51 Å^{-1}) was assessed and subtracted, as shown in *Figure 6(b)*. The validity of this assumption will be discussed in the result section.

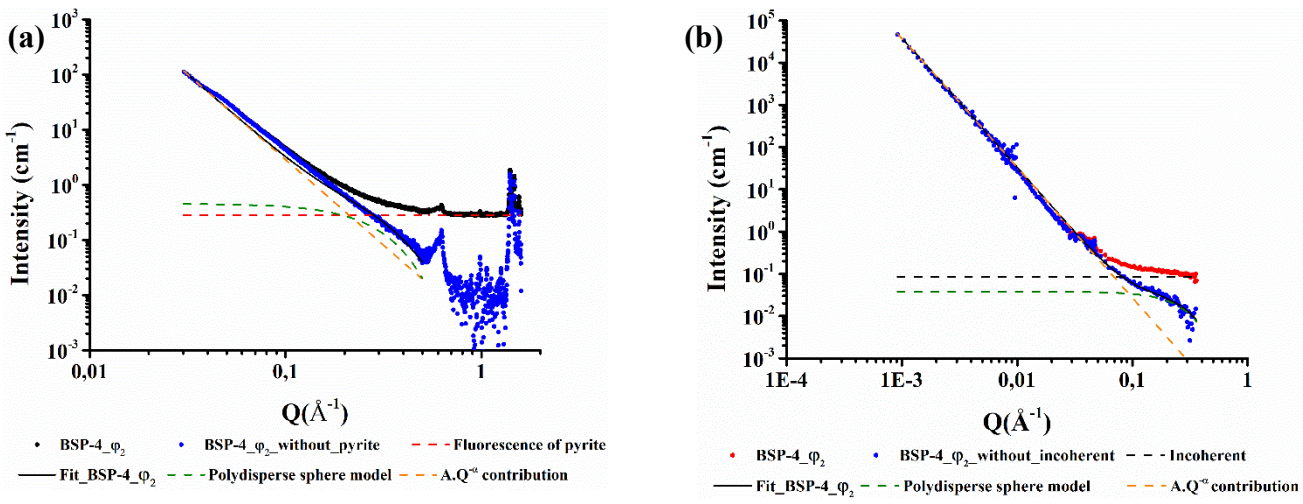

Figure 6. *(a) Example of fluorescence subtraction on BSP-4_φ_2 SAXS data. (b)Example of incoherent subtraction on BSP-4_φ_2 SANS data. Both scattering profiles are displayed as a function of two contributions, log normal (dark green dash lines) and A.$Q^{-\alpha}$ (orange dash lines).*

2.7.3. Initial scattering profiles treatment. Two types of data integrations were performed on scattering 2D anisotropic pattern, as shown in *Figure 7*. As defined earlier, studied source rocks are laminated rocks. It is then possible to measure a 2D scattering pattern being anisotropic. Consequently, radial average of 2D pattern was realized using two angular sectors as illustrated in *Figure 7(a)*. The first sector φ_1 is defined by the angle $\varphi = 90°$ along the elongated part of the anisotropic pattern with an aperture angle of $\Delta\varphi = 60°$. The other one φ_2 is normal to the angle φ_1 as $\varphi_1 + 90°$ and $\Delta\varphi = 60°$. Obtained scattering curves, displayed in *Figure 7*(c), exhibit the scattering intensity as a function of the wave vector Q.

The anisotropic 2D scattering patterns suggest that in the system some scatterers are preferentially oriented along one direction. Thus, scattering patterns were also azimuthally averaged according to two distinct regions, as shown in *Figure 7(b)*. The first one, S_1, is at low Q values, $5.10^{-2} < Q < 0.2$ Å^{-1}, and the second region, S_2, is in high Q-region, $0.34 < Q < 0.5$ Å^{-1}. From the 1D curve, illustrated in *Figure 7(d)*, the variation of the scattering intensity is plotted as a function of the azimuthal angle φ from 0° to 360° with an aperture step angle of 5°. As particles are oriented, the scattering intensity

gives information on the main orientation of particles and on the sample structure. The order parameter *S* – denoted sometimes the Herman's parameter - quantifies the material anisotropy and is used frequently in nematic crystal and clays domains.[64-67]

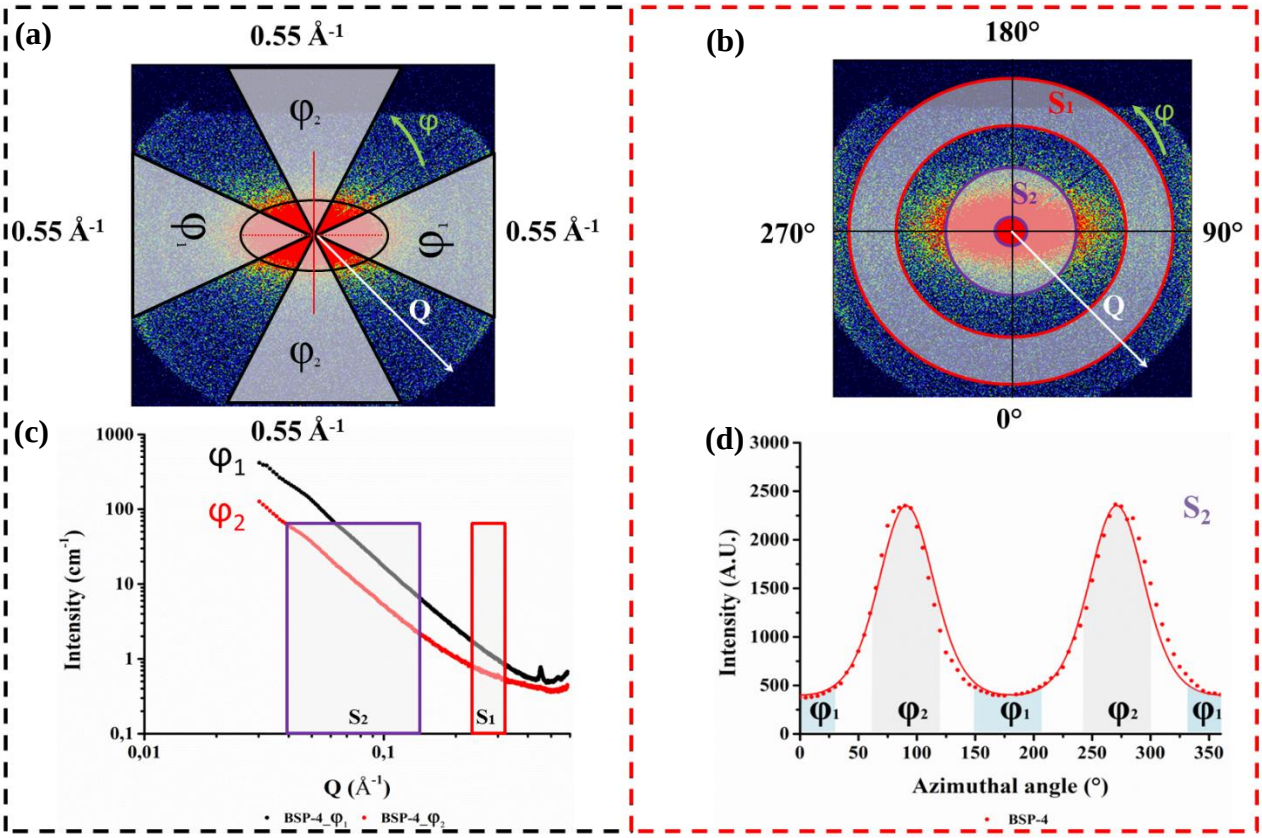

Figure 7. *2D pattern area of interest according to radial (a) and azimuthal (b) average and their scattering intensities (c) and (d).*

One popular way to fit anisotropic SAXS data is to use, for a small *Q* range, the Maier-Saupe function[68,69] defined as :

$$f(\varphi) = A + B.exp(m.cos^2((\varphi - \psi) * \left(\frac{\pi}{180}\right))) \quad (2)$$

Where A is the flat background, B is a multiplier coefficient, m accounts for the particle orientation, φ is the azimuthal angle and ψ is the maximum of intensity. Then, the Maier-Saupe data are normalized to their area, to compare results obtained for each sample, according to :

$$\boldsymbol{A} = \int_{0}^{\pi} \boldsymbol{f(\theta).sin(\theta)\, d\theta} \tag{3}$$

and

$$\boldsymbol{f(\theta)_{norm}} = \frac{\boldsymbol{f(\theta)}}{\boldsymbol{2\pi.A}} \tag{4}$$

With θ the normal to the angle between the particle and the laboratory frame z axis.

Afterward, the order parameter S is expressed as the mean of a second-order Legendre polynomial :

$$\boldsymbol{S} = \langle \frac{\boldsymbol{3.cos^2(\theta) - 1}}{\boldsymbol{2}} \rangle \tag{5}$$

And integrated over the whole solid angle $\sin(\theta)\,.\,d\theta.\,d\varphi$:

$$\boldsymbol{S} = \int_{0}^{2\pi} \boldsymbol{d\varphi} \int_{0}^{\pi} \boldsymbol{f(\theta)_{norm}}.\frac{\boldsymbol{3.cos^2(\theta) - 1}}{\boldsymbol{2}}.\boldsymbol{\sin(\theta)\, d\theta} \tag{6}$$

The order parameter values range from 0, isotropic media, to 1, perfectly oriented particles as columnar or smectitic crystal-liquid phases.[66]

3. RESULTS

3.1. Frame of Scattering modeling

Scattering intensities being related to the so called Scattering Length Densities (SLD) fluctuations, we first examined what are SLD in source rocks for both neutron and X-ray and secondly how SLD may be taken into account in intensities modeling.

3.1.1. Scattering Length Densities

The SLD of a component or a phase is related to its elemental composition and to the type of radiation used. For each component, SLD is calculated according to the formula:[20,21,27,28,70]

$$\boldsymbol{\rho} = \frac{\mathbf{1}}{\boldsymbol{V}} \sum_{\boldsymbol{i}} \boldsymbol{n_i b_i} \tag{7}$$

Where V is a volume representative of the component, n_i the number of atoms of type i contained in the volume V and b_i the atomic scattering length. The latter are tabulated for neutrons in the NIST Database (https://www.ncnr.nist.gov/resources/n-lengths/), whereas they are estimated for X-ray according to $b_i = 0.282.10^{-12} Z_i$ (cm) where Z_i is the atomic number of atoms of type i. For a mixture of components, the mean SLD, $\langle\rho\rangle$, for both radiation beam is established according to:

$$\langle\boldsymbol{\rho}\rangle = \sum_{\boldsymbol{j}} \boldsymbol{\phi_j \rho_j} \tag{8}$$

With $\sum_j \phi_j = 1$, ϕ_j the volume fraction of the component j and ρ_j the SLD of the component j.

From FESEM observations, three different phases are observed : mineral, kerogen and pores.

Minerals :

The SLD of the main minerals in our samples are reported on *Table 3*.

Table 3. *neutron and X-Ray SLD values of minerals. (a) Data coming from the mineralogical database webmineral, on : http://webmineral.com/*

Phase	Chemical formula[a]	Density[a] (g/cm^3)	SLD X-rays ($x\ 10^{10}\ cm^{-2}$)	SLD Neutrons ($x\ 10^{10}\ cm^{-2}$)
Quartz	SiO_2	2.65	22.5	4.2
Albite	$NaAlSi_3O_8$	2.62	22.1	4.0
Muscovite	$KAl_2(AlSi_3O_{10})(OH)_2$	2.90	24.5	3.9
Illite	$K(Al,Fe,Mg)_2(Si,Al)_4O_{10}(OH)_2$	2.75	23.1	3.7
Calcite	$CaCO_3$	2.71	23.0	4.6
Dolomite	$CaMg(CO_3)_2$	2.87	24.3	5.4
Apatite	$Ca_5(PO_4)_3(OH,F,Cl)$	3.19	26.9	4.1
Pyrite	FeS_2	4.93	40.5	3.7

For neutrons, minerals SLD are close to each other (~ 4.10^{10} cm^{-2}) which allows to consider minerals as a homogeneous phase. The corresponding mean value is easily assessed using Equation 8 with volume fraction of each mineral determined by XRD. For X-rays, most of the minerals have a SLD value close to 24.10^{10} cm^{-2}, except pyrite. Thus, X-ray perceives the minerals as two distinct phases since differences in SLD give rise to a contrast.

Kerogen:

Kerogen in analogous materials such as coal,[7] is described as a homogeneous phase where its SLD is similar whatever the macerals type.

Since our sample selection was designed to obtain a continuous sequence of increasing maturity, it is mandatory to consider the effect of maturity on kerogen SLD. A recent study on kerogen in source rocks,[71] show that neutron kerogen SLD vary from 1.10^{10} cm^{-2} for immature kerogen up to 4.10^{10} cm^{-2} for the overmature one. Elemental compositions and densities of gas shale from various maturities and

369 after acid attack, given by Thomas and coworkers (2014),[71] were used here to assess neutron and X-
370 ray SLD as well as mass densities of kerogens. Thus, we assumed that all the Fe content in attack acid
371 residues is only due to pyrite FeS_2. The pyrite contribution, including the sulfur one, has been
372 subtracted to obtain elemental composition and densities of model kerogens containing C, H, O and N
373 atoms. X-ray and neutron SLD were assessed using Equation 7. Results are plotted on *Figure 8* as a
374 function of kerogen densities. Indeed, kerogen density vary in the same way as vitrinite reflectance
375 and could be used as a maturity index.

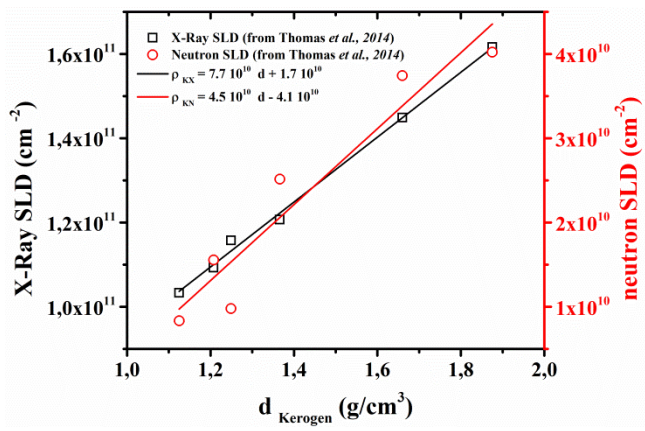

376 ***Figure 8.*** *X-ray and neutron kerogen SLD as a function of kerogen densities based on data from*
377 *Thomas et al., 2014.*[71] *X-ray linear regression (black curve) and neutron linear regression (red curve)*
378 *for kerogen SLD estimations.*

379 Linear regressions were performed on kerogen X-ray and neutron SLD. From these linear
380 regressions, ρ_{KN} and ρ_{KX} can be expressed as :

$$\boldsymbol{\rho_{KN}} = 4.5.10^{10}.d - 4.1.10^{10}$$

381 (9)

382 and $$\boldsymbol{\rho_{KX}} = 7.7.10^{10}.d + 1.7.10^{10}$$

383 with ρ in cm^{-2} and d in g/cm^3.

384 (10)

Pore space :

For this study, four model fluids are considered : air, methane in gaseous form, toluene and pentane. SLD values are listed in *Table 4* below.

Table 4. *Model Fluids SLD calculated from equation 7.*

Model fluids	**Neutrons SLD** ($x\ 10^{10}\ cm^{-2}$)	**X-Ray SLD** ($x\ 10^{10}\ cm^{-2}$)
Toluene	0.9	8.0
Pentane	-0.6	6.2
$Methane_{(g)}$	0.0	0.0
Air	0.0	0.0

Pores can be fulfilled by gaseous species and/or by condensed hydrocarbons. If the pore space is fulfilled by a gas, its SLD for both X-ray and neutron is close to 0. If condensed fluids are in the pore space, it is then assumed that neutron SLD is almost null as condensed fluids have a SLD value ranging from 1.10^{10} cm^{-2}, for aromatic fluids, to -0.5 10^{10} cm^{-2} for aliphatic fluids. For X-ray, pore space SLD will be close to 8.10^{10} cm^{-2} for aromatics fluids and around 6.10^{10} cm^{-2} for aliphatic fluids.

From these different SLD values, it appears that since neutron overmature kerogen and minerals SLD values are close, neutron scattering acquired on overmature gas shales could be interpreted in the frame of a two-phases system. As shown in *Figure 8*, for immature and mature kerogen, SLD values are much lower than the SLD of the mineral phase. Consequently, the two-phase system, which is classically used to described source rock scattering data, is less relevant than a three-phases one. Concerning the nature of pore content, it is clear that neutron cannot distinguish gas from hydrocarbons whereas X-ray can. For X-ray SLD values, four phases have different SLD : pyrite,

others minerals, kerogen and pore space. From XRD measurements, pyrite content is low, less than 2.5 vol %, in the studied source rocks. Moreover, FESEM observations reveals that a large part of pyrite is present as grains with sizes higher than 1 µm. These grains will contribute to X-ray scattering in a Q range that is not probed by our instrument. Firstly, pyrite is therefore neglected and its contribution will be discussed after data modeling. Hence, for both types of radiation, at least three SLD values has to be considered rather than a two-phase approximation.

3.1.2. Scattering intensity. As shown in FESEM observations, samples are described as a four phases system : pyrite, other minerals, kerogen and pores. Even if pyrite is discarded, we will distinguish for scattering four phases, namely minerals, kerogen, pores included in kerogen and pores in minerals. For that purpose, source rocks system can be defined as follows:

$$\sum_{i=1}^{4} \boldsymbol{H_i(\vec{r})} = \boldsymbol{H_M(\vec{r})} + \boldsymbol{H_K(\vec{r})} + \boldsymbol{H_P(\vec{r})} + \boldsymbol{H_{P'}(\vec{r})} = \mathbf{1} \tag{11}$$

Where $H_M(\vec{r})$, $H_K(\vec{r})$, $H_P(\vec{r})$ and $H_{P'}(\vec{r})$ are respectively, the characteristic functions of the minerals, the kerogen, the pores contained in the kerogen and the pores in minerals. From previous equation, the amplitude $A(Q)$ of neutrons or X-ray can be written as :

$$\boldsymbol{A(Q)} = \int_V \left[\sum_{i=1}^{4} \boldsymbol{\rho_i H_i(\vec{r})} \right] \boldsymbol{e^{-iqr}} \tag{12}$$

Since $\sum_{i=1}^{4} H_i(\vec{r}) = 1$ and fluctuations of SLD occur, an arbitrary SLD reference can be chosen to determine $\rho_i H_i(\vec{r})$ in regard to the phase of interest, the kerogen, as :

$$\sum_{i=1}^{4} \boldsymbol{\rho_i H_i(\vec{r})} = (\boldsymbol{\rho_M} - \boldsymbol{\rho_K})\boldsymbol{H_M(\vec{r})} + (\boldsymbol{\rho_P} - \boldsymbol{\rho_K})\boldsymbol{H_P(\vec{r})} + (\boldsymbol{\rho_{P'}} - \boldsymbol{\rho_K})\boldsymbol{H_{P'}(\vec{r})} + \boldsymbol{\rho_K}$$

(13)

$A(Q)$ can be rewritten according to the phase of interest through the Fourier transform. We note that the Fourier transform of ρ_K is a dirac centered at $Q = 0$ and do not appear in the amplitude expression:

$$\boldsymbol{A(Q) = (\rho_M - \rho_K)\widetilde{H_M}(R) + (\rho_P - \rho_K)\widetilde{H_P}(R) + (\rho_{P'} - \rho_K)\widetilde{H_{P'}}(R)}$$

(14)

From $A(Q)$, the scattering intensity is expressed according to $I(Q) = A(Q)A(Q)^*$.[74] The crossed terms are considered negligible owing to FESEM observations revealing no correlation between the kerogen and the pores contained in the mineral matrix. Arthur and Cole (2014) have shown by a FESEM/FIBSEM dual beam analysis that the mesopores are mainly contained in the organic matter. In addition, Bazilevskaya and coworkers (2015) demonstrated that about 50% of the porosity cannot be observed by direct space analysis and may be contained in the organic matter or the interlayer of clayey minerals. Thus, the scattering intensity is expressed as :

$$\boldsymbol{I(Q) = (\rho_M - \rho_K)^2\widetilde{H_M}(Q)\widetilde{H}^*_M(Q) + (\rho_{P'} - \rho_K)^2\widetilde{H_{P'}}(Q)\widetilde{H}^*_{P'}(Q) + \left(\rho_p - \rho_K\right)^2\widetilde{H_P}(Q)\widetilde{H}^*_P(Q)}$$

(15)

At this point, the scattering intensity as illustrated in *Figure 6* can be described as the sum of three contributions depending on a four phase system which are defined using three terms of contrast.

The first contribution is related to the contrast between mineral and kerogen phases. Based on FESEM observations, kerogen is in the form of micrometric to nanometric domains and its volume fraction, related to the TOC content, is few percent. A strong scattering intensity at small Q values is then expected for this contribution. Indeed, at low Q values, the curve trend appears to be a power law which can be expressed as $A.Q^{-\alpha}$, with α close to 3, A being a prefactor explicited later. In source and sedimentary rocks studies, the α exponent is sometimes related to a surface fractal dimension Ds by $\alpha = 6 - Ds$ where Ds is restricted to $2 < Ds \leq 3$.[75-77] Schmidt (1982),[78] shows that the α exponent

could be also related to power law size distribution $f(R) \sim R^{-(1-Ds)}$. Whatever the physical meaning of power law intensity dependence, we will consider α as a fitting parameter and concentrate on the prefactor A that could be expressed as the product of squared contrast factor $(\rho_M - \rho_K)^2$ by a factor a related to the structural arrangement of kerogen in the mineral matrix. Hence, the first term of Equation 15 would be $a(\rho_M - \rho_K)^2\, Q^{-\alpha}$

The second contribution, as highlighted by the FESEM characterizations, is related to pores in mineral phases, which are mainly macropores diluted within the mineral matrix. The mineral/pores interface seems to be smooth and their sizes vary from macrofractures to macropores. Consequently, their contribution likely follows a Porod behavior ($I(Q) \sim Q^{-4}$) which starts at lower Q values and strongly decreases toward higher Q values. At least, this means that this contribution to $I(Q)$ is negligible in the high Q domain probed.

The last contribution is related to the distribution of micropores in the kerogen matrix. As pores shape and size couldn't be well defined, owing to limitations (resolution and/or statistical representativeness), by direct space analysis such as FESEM or transmission electron microscopy, it is assumed that pores have a variety of shape and size as source rocks are natural materials. Both assumptions lead to a smoothing of the scattering curve compared to unique size and shape pores and make difficult to deconvolute both effects. In this study, we fixed the shape of the considered objects as spherical for sake of simplicity and assumed that size are distributed. This assumption preserve the physical meaning of the average size of the pores and it associated volume fraction. In source rocks the pore size distribution is often considered as peaked like in gas adsorption/desorption[17,27,28,41] or NMR[34,46] analysis. The $\widetilde{H_P}(Q)\widetilde{H}_P^*(Q)$ term is expressed as $n\int_{R_{min}}^{R_{max}} f_P(R)V_P^2(R)P(Q,R)\,dR$ - a diluted dispersion of pores - where n is the number density of pores, $V_p(R)$ stand for the volume of pore of size

465 R, $P(Q,R)$ is the form factor of the pores ($P(0,R)$ = 1) chosen here as spherical, and $f_P(R)$ the
466 normalized number size distribution function chosen here for convenience as log normal :

$$\boldsymbol{f_P(R) = \frac{1}{\sigma\sqrt{2\pi}}\exp(-\frac{ln\,(R/\mu)^2}{2\sigma^2})}$$

467 (16)

468 Where μ the mean value of sphere radius and σ the size polydispersity.

469 Accordingly, for the scattering vector range measured in this study, a three-phase system with two
470 main contributions, is defined and expressed, for X-rays (X) and neutrons (N) as :

$$\boldsymbol{I(Q)_{X,N} = a(\rho_M - \rho_K)^2_{X,N}\, Q^{-\alpha} + n(\rho_P - \rho_K)^2_{X,N} \int_{R_{min}}^{R_{max}} f_P(R) V_P^2(R) P(Q,R)\, dR}$$

471 (18)

472 In this equation, parameters giving a direct influence on the intensity Q dependence, namely α, σ
473 and μ, should be retrieved separately by fitting procedures. They provides details on each contribution
474 prevailing in different Q domains. By contrast, only global prefactors $A = a(\rho_M - \rho_K)^2$ and $N =$
475 $n(\rho_P - \rho_K)^2$ that adjust the amplitude of each Q dependence, will be extracted from the modeling.

476

477 **3.2. Anisotropy**

478 First, we consider the $I(Q)$ behavior for the two azimuthal sectors φ_1 and φ_2 according to *Figure*
479 *7*(a). Both scattering techniques results are illustrated in *Figure 9* for SANS and in *Figure 10* for
480 SAXS/WAXS. It is noted that the MT-1 sample gives isotropic 2D pattern. As detailed in the
481 literature, scattering data on source rocks follow at small Q values an algebraic trend assimilated to
482 $A.Q^{-\alpha}$.[8,20-23,27,35,71,79,80] In both techniques, the α parameter, reported in *Table 6*, have similar values
483 close to 3 and the intensity ratio between φ_1 and φ_2 remains constant until a breakdown around 0.03 Å^{-}

^{1} in SANS and 0.1 Å^{-1} in SAXS/WAXS. For larger Q values the scattering intensity is quite similar whatever the azimuthal sector. This behavior is ascribed to :

- anisotropic scattering at small Q values likely due to preferential orientation of low dimensionality particles such as clays and micas.

- isotropic scattering at large Q values reminiscent of spherical nanopores located in the kerogen

A further confirmation of this attribution is shown in supplementary information where the high Q intensity signal is ranked as the one of TOC content.

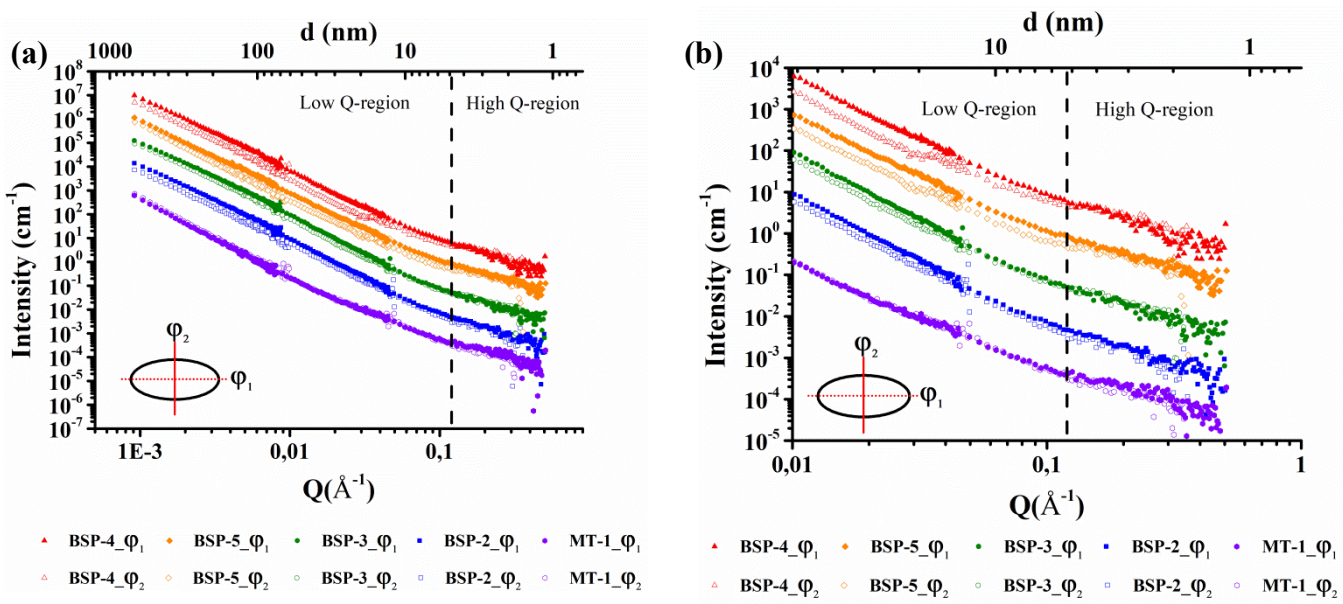

Figure 9. *(a) Samples SANS profiles according to the azimuthal area of interest. Full dots represent data obtained for $\varphi_1 = 0°$ and empty dots are data coming from $\varphi_2 = 90°$. (b) Zoom on SANS profiles to match the Q-range of SAXS/WAXS data. In both graphs, SANS profiles of MT-1, BSP-2, BSP-5 and BSP-4 are scaled vertically according to the scale factors 0.01, 0.1, 10 and 100, respectively.*

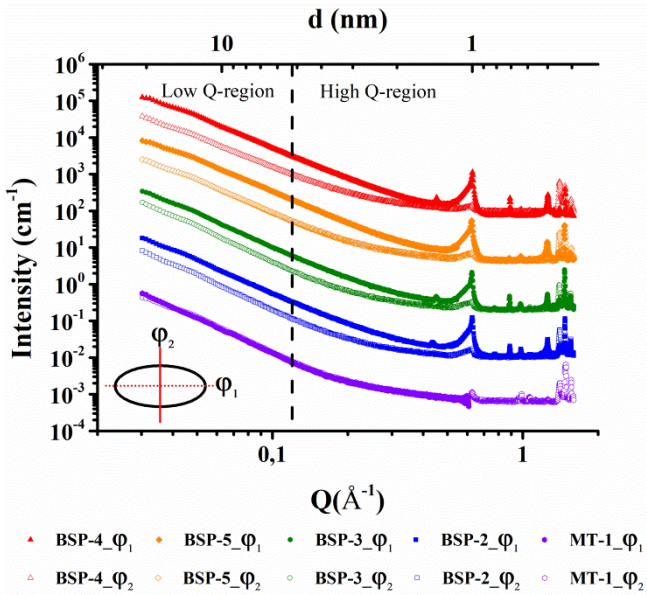

Figure 10. *(a) Samples SAXS/WAXS profiles according to the azimuthal area of interest. Full dots represent data obtained for $\varphi_1 = 0°$ and empty dots are data coming from $\varphi_2 = 90°$. SAXS/WAXS profiles of MT-1, BSP-2, BSP-5 and BSP-4 are scaled vertically according to the scale factors 0.003, 0.05, 15 and 300, respectively.*

Secondly, we consider the *I(φ)* behavior in the two *Q* ranges *S1* and *S2* according to *Figure 7(b)*. Samples data (dots) and fitting curves (lines) to the Maier-Saupe function (Equation 1) are illustrated in *Figure 11(a)* for low *Q*-region and *Figure 11(b)* for high *Q* values. At first sight, from MT-1 to BSP-4 samples an increasing intensity and sharpness of the distribution along the azimuthal angle is observed in both regions. Three groups are distinguished, the MT-1 isotropic sample with a flat intensity, the BSP-2/BSP-3 group exhibiting a broad distribution and the BSP-4/BSP-5 which have the highest and sharper distribution. In the *Figure 11(b)*, as the BSP-5 sample does not possess chlorite in SAXS profile, its intensity along the azimuthal angle is smaller than for BSP-4.

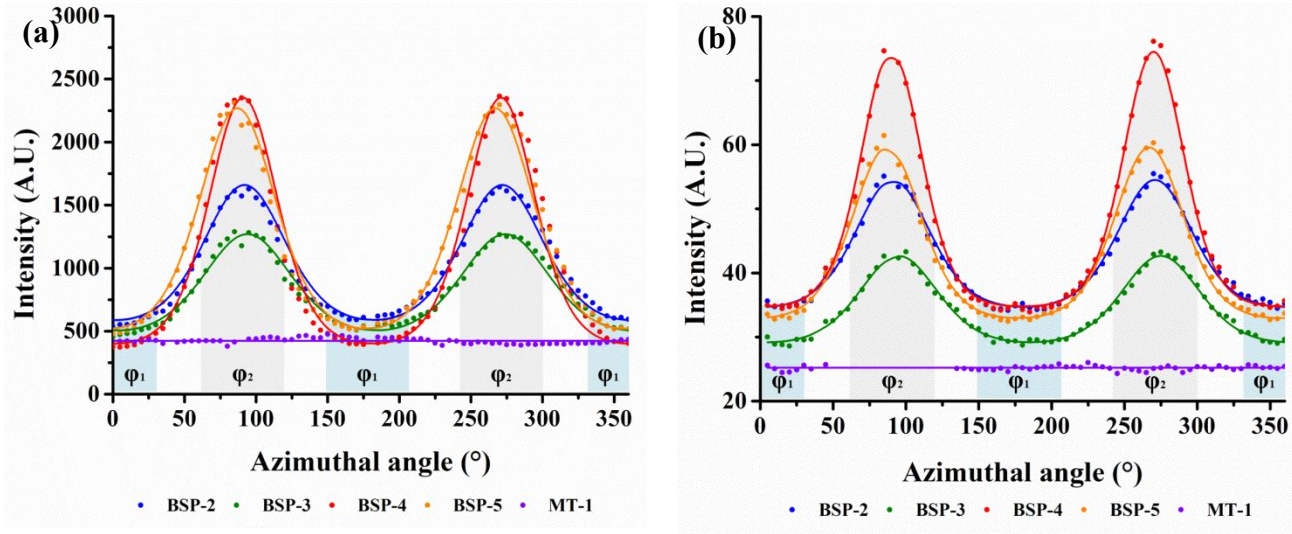

Figure 11. *SAXS azimuthal integration profiles of BSP and MT samples within (a) low Q-region ($Q = 5.10^{-2}$ to 0.2 $Å^{-1}$) and (b) high Q-region ($Q = 0.34$ to 0.5 $Å^{-1}$). Integrated azimuthal angle regions from profiles decomposition are illustrated by the light blue and light grey areas respectively for φ_1 and for φ_2.*

As shown in *Table 5*, it is possible from these data, to apply the Maier-Saupe fitting function to extract A, B, m and ψ parameters and then to calculate the order parameter S. Values of ψ are close to 90° suggesting that anisotropic particles align preferentially with their long axis parallel to the bedding plane. Order parameters for BSP samples at low Q values are ranking from 0.13 and 0.14, for BSP-3 and BSP-2, up to 0.21 and 0.26, for BSP-5 and BSP-4. Whereas, in the high Q-region, this parameter is quite low, barely reaching 0.09 at its maximum for BSP-4. BSP-2 and BSP-3 exhibit the lowest values with S = 0.06. Then, BSP-5 have an order parameter of 0.08. This seems to indicate that this part of the signal is less anisotropic and is dominated by an isotropic pattern. For MT-1, as its 2D scattering pattern is isotropic, S parameters for both Q regions is equal to 0.

521 ***Table 5.*** *Maier-Saupe function parameters determined on SAXS profiles and their calculated S*

522 *parameter for low Q-region (Q = 5.10^{-2} to 0.2 Å^{-1}) and high Q-region (Q = 0.34 to 0.5 Å^{-1}).*

Reference	Low Q region : 5.10^{-2} to 0.2 Å^{-1}					High Q region : 0.34 to 0.5 Å^{-1}				
	A	B	m	ψ	S	A	B	m	ψ	S
BSP-2	418.6	168.8	2.0	92	0.14	28.6	4.4	1.8	91	0.06
BSP-3	324.8	181.1	1.6	94	0.13	22.6	5.6	1.4	95	0.06
BSP-4	304.1	96.6	3.1	91	0.26	32.3	1.1	3.6	90	0.09
BSP-5	342.1	177.1	2.4	87	0.21	28.9	2.5	2.5	87	0.08
MT-1	423.4	0.0	0.0	0.0	0.0	24.7	0.0	0.0	0	0.0

523

524 The separation of the global signal into an anisotropic and an isotropic contribution allows to specify

525 a more accurate expression for *Q* dependence of intensity :

526 $$\boldsymbol{I(Q)_{X,N} = a(\varphi)(\rho_M - \rho_K)^2_{X,N}\, Q^{-\alpha} + n(\rho_P - \rho_K)^2_{X,N} \int_{R_{min}}^{R_{max}} f_P(R) V_P^2(R) P(Q,R)\, dR}$$

527 (19)

528 where the prefactor *a* has been substituted by *a(φ)*.

529

530 **3.3. Multiscale structure.**

531 We took advantage of anisotropic scattering to consider, in the fitting procedure based on equation

532 19, the data acquired in azimuthal sector φ_2. Indeed, for this sector, the scattering intensity from the

533 first term of equation 19 is minimized and allows to better evaluate the second term contribution that

534 remain moderate. This strategy could be optimized by considering a much smaller angular sector $\Delta\varphi_2$

535 but it would require much larger acquisition time. Hence, SANS and SAXS/WAXS "φ_2" data related

536 to the five source rocks were fitted to equation 19 by using *SASFit* software.[81] Results represented in

537 *Figure 12(a)* for SANS data and in *Figure 12(b)* for SAXS/WAXS measurements shows a good

538 agreement between model and data for the both radiation on the whole Q range. Geometrical
539 parameters (α, μ and σ), reported in *Table 6*, are first assessed by fitting SANS data as the Q
540 dependence of these latter are more pronounced than for SAXS data. Then, modelling was performed
541 based on a simultaneous scattering fit of SAXS/SANS data to obtain the pre-factors $a(\rho_M - \rho_K)^2$ and
542 $n(\rho_P - \rho_K)^2$, containing the SLD of each phase and depending on the type of radiation.

543 Results obtained for geometrical parameters indicate that both SANS and SAXS/WAXS scattering
544 intensity can be described as the sum of two types of contributions using the same parameters giving
545 the Q dependence, namely α, μ and σ. These results also validate the SANS incoherent scattering
546 background subtraction based on mean value measured at high Q values .

547 The α parameters, that are close to each other (3.1 – 3.25) for BSP samples and slightly higher (3.4)
548 for MT1, are in the range of reported values.[8,10,14,20,23,27,28,35,39,79] The widths σ of nanopore size
549 distributions are quite narrow, always close to 0.2 and the fitted parameters given here are obtained
550 with values of σ set to 0.2 for a better visibility. The mean radius of nanopores is close to 0.5 nm, a
551 value commonly found for this type of material.[20,79] For the overmature sample, the curves at high Q
552 values show clearly two separate bumps assigned here to two pore size distributions. The first one has
553 a mean radius of 0.5 nm in the same range as the mature samples and the second one has much higher
554 values close to 3.5 nm. In addition, it appears that SAXS techniques can also provide information on
555 porous media in the kerogen phase as both SANS and SAXS/WAXS profiles are in good agreement
556 using pore size define from SANS modeling. From fitting data, BSP samples are described as source
557 rocks with pore radii varying from 0.5, for BSP-3, BSP-4 and BSP-5, up to 0.7 nm, for BSP-5. MT-1
558 sample displays two pore radii 0.5 nm and 3.5 nm. In addition, fit sensitivity on the pore size radius
559 was tested as shown in supplementary information. It shows that radii nanopore measurements are
560 sensitive within ~ 1-2 Å range.

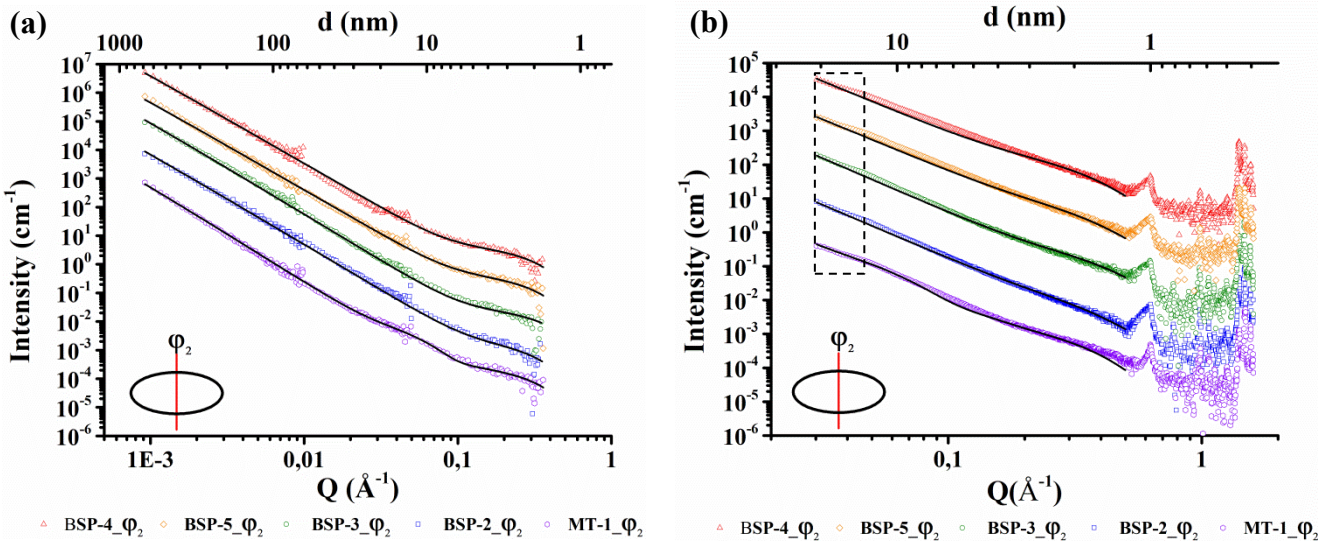

Figure 12. *(a) Samples SANS and fit profiles coming from data integrated along the azimuthal angle $\varphi_2 = 90°$. SANS profiles of MT-1, BSP-2, BSP-5 and BSP-4 are scaled vertically according to the scale factors 0.01, 0.1, 10 and 100, respectively. (b) Samples SAXS/WAXS and fit profiles from data acquired along the azimuthal angle $\varphi_2 = 90°$. SAXS/WAXS profiles of MT-1, BSP-2, BSP-5 and BSP-4 are scaled vertically according to the scale factors 0.003, 0.05, 15 and 300, respectively. In both graphs, solid lines represent the sum of $f(R)$ and $f_P(R)$ contributions determined with SASfit software.*

Table 6. *Fitting parameters of SANS and SAXS data obtained for the α parameter and the term of contrast $A = \alpha(\varphi)\left(\rho_M - \rho_K\right)_N^2$ related to the $A.Q^{-\alpha}$ contribution and also the radius (μ) and the term of contrast $n(\rho_P - \rho_K)_N^2$ related to the log normal contribution.*

Reference	α	mu (nm)	Neutrons $\alpha(\varphi)(\rho_M - \rho_K)_N^2$	Neutrons $n(\rho_P - \rho_K)_N^2$	X-rays $\alpha(\varphi)(\rho_M - \rho_K)_N^2$	X-rays $n(\rho_P - \rho_K)_N^2$
BSP-2	3.20	0.7	4.4	0.6	4.9	0.6
BSP-3	3.25	0.5	3.4	4.4	4.4	3.5
BSP-4	3.10	0.5	6.4	3.6	7.2	5.6
BSP-5	3.10	0.5	7.6	6.3	11.0	5.2

MT-1	3.40	0.5	0.4	4.0	1.2	6.2
		3.5		9.0		2.9

Regarding the prefactors, we first consider their ratios R_A and R_N since they depend only on squared contrast terms.

$$\boldsymbol{R_A} = \frac{\boldsymbol{A_{\varphi,N}}}{\boldsymbol{A_{\varphi,X}}} = \frac{\boldsymbol{a(\varphi_2)(\rho_{MN} - \rho_{KN})_N^2}}{\boldsymbol{a(\varphi_2)(\rho_{MX} - \rho_{KX})_X^2}}$$

and

$$\sqrt{\boldsymbol{R_A}} = \frac{\boldsymbol{(\rho_{MN} - \rho_{KN})_N}}{\boldsymbol{(\rho_{MX} - \rho_{KX})_X}}$$

$$\boldsymbol{R_N} = \frac{\boldsymbol{N_N}}{\boldsymbol{N_X}} = \frac{\boldsymbol{n(\rho_{PN} - \rho_{KN})_N^2}}{\boldsymbol{n(\rho_{PX} - \rho_{KX})_X^2}} \qquad \text{(20a, 20b \& 21)}$$

The equation 20b, together with the equations 9 and 10 relating the neutron and X-ray kerogen SLD to the kerogen density *d*, form a system of three equations with three unknown (ρ_{KN}, ρ_{KX} and *d*) that could be easily solved. The extracted parameters are reported on *Table 7* for samples of various maturity. It appears that the extracted densities are quite similar – about 1.65 g/cm^3 – for the BSP samples and markedly different – 1.74 g/cm^3 – for the MT1. It points out that BSP samples are mature and MT1 overmature source rock as expected from Rock-Eval pyrolysis measurements (section 2.3.). Regarding the neutron SLD, the one of overmature source rock – 3.7.10^{10} cm^{-2} – is quite similar to the one of mineral, suggesting that the scattering data could have been interpreted in the frame of a two-phase system. Conversely, the neutron SLD differences between minerals and kerogen for the mature source rocks are noticeable (0.5 – 0.7.10^{10} cm^{-2}), justifying the three phases approximation developed here. Regarding X-ray, the large differences between minerals and kerogen SLD show clearly that the three-phase approximation is mandatory to interpret properly SAXS measurements.

Table 7. *Values for ρ_{MN} and ρ_{MX} are calculated from equation 7. Kerogen densities, ρ_{KN}, ρ_{KX} and ρ_{PX} are estimated from, respectively, equation 21, 9, 10 and 22. Estimated n values for kerogen pores and the associated volume fraction.*

Sample	mu (nm)	n (x 10^{19} cm^{-3})	Volume fraction (x 10^{-2})	Kerogen density *d* (g/cm^3)	ρ_{MN} (x 10^{10} cm^{-2})	ρ_{MX} (x 10^{10} cm^{-2})	ρ_{KN} (x 10^{10} cm^{-2})	ρ_{KX} (x 10^{10} cm^{-2})	ρ_{PX} (x 10^{10} cm^{-2})
BSP-2	0.7	0,5	1.0	1.66	4.0	21.3	3.4	14.5	4.3
BSP-3	0.5	4.7	3.0	1.67	4.0	21.3	3.4	14.6	5.1
BSP-4	0.5	6.0	3.8	1.59	3.7	20.3	3.0	14.0	4.4
BSP-5	0.5	5.7	3.6	1.65	3.8	20.2	3.3	14.4	4.9
MT-1	0.5	2.6	1.6	1.74	4.1	21.6	3.7	15.1	0
MT-1	3.5	7.10^{-4}	0.15	-	-	-	-	-	0

Knowing kerogen SLD for both SAXS and SANS techniques, R_N ratios may provide fluids in place SLD values assuming $\rho_{PN} \sim 0$. Then, ρ_{PX} can be expressed as :

$$\boldsymbol{\rho_{PX}} = \frac{-\boldsymbol{\rho_{KN}} + \sqrt{\boldsymbol{R_{2N}}}\boldsymbol{\rho_{KX}}}{\sqrt{\boldsymbol{R_N}}} \tag{23}$$

Calculated ρ_{PX} values are listed in *Table 7* and displayed two different values. For BSP samples, a ρ_{PX} values ranging from $4.3.10^{10}$ cm^{-2} up to 5.10^{10} cm^{-2} are estimated. This value can be attributed to either light condensed hydrocarbons with SLD values smaller than pentane SLD ($6.2.10^{10}$ cm^{-2}), or to a mixture of pores fulfilled by a fluid and empty pores. For the overmature MT1 sample, a value of 0 is found for the nanopores (0.5 nm) population and a value slightly negative for the mesopore (3.5 nm) population. The agreement with both a meaningful (positive) ρ_{PX} value and the best fit intensities gives a null value for mesopores SLD. Hence, for the overmature sample, nano- and meso- pores in

kerogen are considered as empty in full agreement with Sh0 and Sh1 values found with Rock-Eval pyrolysis measurements.

From the prefactors $n(\rho_P - \rho_K)^2_{X,N}$ and the SLD values, the number density of pores n were easily assessed and their values are reported in *Table 7*. The nanopores volume fraction ϕ can be inferred from their number density n and their size distribution using $\phi = n\ 4/3\ \pi <R^3>$, where $<R^3>$ is the third moment of the size distribution that can be calculated analytically for the lognormal distribution. Numerical values are reported in *Table 7*. They are in the range 1-4% and rank roughly like the TOC content.

Concerning the pyrite influence on SAXS data, calculated intensities for BSP-4 and MT-1 samples, which exhibit the highest pyrite content (2.3 and 2.5 %vol), display the higher discrepancy with measured intensities in the Q range around 0.1 $Å^{-1}$. This discrepancy is clearly ascribed to pyrite content that gives an additional intensity contribution. If intensity modeling is still acceptable for these samples, it is clear that for samples containing higher pyrite contents, the fitting procedure will give meaningless parameters, especially for the mesopores SLD. Hopefully, the other estimated parameters would stay unaffected by pyrite.

4. DISCUSSION

Source rocks is one of the most difficult material to characterize. Indeed, they are multiphase systems (minerals, solid organic matter and pore space filled by various liquid or gaseous hydrocarbons) and the relevant length scales extend from sub-nanometer for nanopores included in kerogen up to few microns for minerals or kerogen domains. Moreover, they are natural materials with inherent composition variability and laminated rocks where bedding could induce a structural orientation leading to anisotropy of properties. Based on these considerations, sample preparation is

629 one of the major concern when studying such materials. Complementary scattering techniques are
630 chosen here for their ability to probe the desired length scales. Herein, an innovative methodology is
631 proposed to overcome (i) composition variability, and (ii) loose of sample integrity and orientation
632 upon grinding. Thin blade samples allows to average several random X-ray scattering measurements
633 in a surface comparable to the section the neutron beam (a 5 mm diameter circular diaphragm). A
634 sample thickness of ~ 200 µm, allow to get usable transmission for both radiation while avoiding
635 multiple scattering. Contrary to scattering measurements on powdered sample[14,20,35,77] or on thin blade
636 section cut parallel to bedding[10,23,27,28] that gives isotropic signal, the thin blades considered here are
637 cut normal to the bedding plane in order to get information on possible structural orientation.[8,82]
638 Finally, this sample preparation allow to compare X-ray and neutron scattering intensities obtained on
639 the same volume and in the same orientation.

640 Quantifying this orientation has to be taken into account when considering fluid flow properties for
641 transport issues or mechanical properties. Indeed, it is well known that bedding structures modify the
642 rock permeability to fluids according to the considered orientation,[8,12,17,83] with values ranging from
643 1.10^{-19} m² to 1.10^{-21} m², for normal to bedding cut, and 1.10^{-21} m² to 1.10^{-22} m², for parallel to bedding
644 cut. In soil science, recent studies evidenced the importance of preferred clay orientation on the
645 diffusional properties of water.[84] Here, order parameter vary from 0 (random orientation) up to ~ 0.3.
646 The random orientation is associated to the coarse grained texture of Montney sample whereas
647 significant values of order parameters are found for fine grained Barnett shales. This striking
648 difference could be the result of various size ratio between low dimensionality particles such as clays
649 or micas and other minerals. Indeed, it has been shown, on model systems of particles mixture
650 (platelets and spheres), that orientation upon sedimentation depend on the diameter ratio.[85] Anisotropic
651 properties are also illustrated by the HS-GC experiment conducted on thin blade sections where the

concentration of thermodesorbed species in the vapor is much larger for normal cut than for parallel cut to the bedding (Supplementary Data).

The quantitative comparisons of X-ray and neutron scattering intensities are based on contrast factor specific to each radiation. The detailed examination of scattering length densities evidence that source rocks could be described for both radiation with three distinct contributions : minerals, kerogen and pores. For overmature kerogens, the neutron scattering could be reduced to the frequently used two phase system approximation, matrix and pores.[8,10,14,20,23,27,28,35,39,79] This two phases model, based on diluted polydispersed pores, is usually applied to retrieve the pore size distribution and the total porosity. Here, considering three phases allow to broaden scattering techniques to low mature kerogens and to X-ray measurements. A corresponding expression of scattering intensities based on two main contributions is developed. The first one is related to the dispersion of kerogen domains in the mineral matrix, which prevails at low Q values, and turns out to be anisotropic. The second one describes a diluted dispersion of nanopores in the kerogen, giving a dominant isotropic signal at large Q values that remains moderate. We took advantage of anisotropy to consider the azimuthal direction where the scattering at low Q is reduced in order to better appreciate the contribution, at large Q values, of kerogen nanoporosity. The three phases model allows to fit both X-ray and neutron data with the same geometric parameters which prove the selectivity of the model. Moreover, the intensity ratio between X-ray and neutron prefactors for each contribution allow to retrieve valuable parameters such as (i) the X-ray and neutron kerogen SLD as well as its mass density, both of them being considered as a maturity index, (ii) the nanopore size distribution, the number density of nanopores and their associated volume fraction, and (iii) the X-ray SLD of nanopores that gives a first approximation on the nature of filling fluids. All these parameters are reachable thanks to quantitative comparison of SANS and SAXS measurements, a strategy commonly applied to solve complex

675 nanostructural order.[86,87] The pyrite has not been taken into account for SAXS modeling and we show
676 that for pyrite content above ~ 2.5 vol %, the SLD of nanopores is suspicious rendering the nature of
677 filling fluid unclear.

678 This methodology has been applied to a series of source rocks with an increasing maturity according
679 to Rock-Eval pyrolysis measurements. For mature samples, the SAXS/SANS analysis show (i) a
680 kerogen mass density of ~1.64 $g.cm^{-3}$ in good agreement with geochemical estimation (ii) a nanopore
681 size radius distribution centered on 0.5-0.7 nm, in agreement with the literature,[20,35, 79,88] with 20% of
682 polydispersity and accounting for pore volume fractions of ~ 0.01 to 0.04. When the volume fraction is
683 compared to the Rock-Eval pyrolysis TOC content (~ 4.5 to 9 % wt), the proportion of pores in
684 kerogen is about a fifth to a half of the kerogen domain. At such pore concentration, the assumption of
685 diluted pores could not always be valid and considering a structure factor *S(Q)* in the intensities
686 modeling should be taken into account. As any peak in the high *Q* region, relative to a short range pore
687 ordering, has been detected, a structure factor rather based on pore aggregates should be considered. It
688 would give additional information on nanopore connectivity relevant for future studies and (iii) an X-
689 ray nanopores SLD of ~ 4 to 5.10^{10} cm^{-2}. These values can account for either condensed (liquid) light
690 hydrocarbons or a mixture of heavier condensed hydrocarbons and empty pores. For the overmature
691 sample, the kerogen mass density is higher (1.74 $g.cm^{-3}$) as expected, the pore size distribution is
692 bimodal with a mode close to the one of mature sample and an additional distribution of mesopores
693 (with a radius of 3.5 nm) accounting for a small pore volume fraction of ~ 0.1-0.2 %. Both porous
694 media are found to be empty in full agreement with almost null values of free hydrocarbons as
695 measured in the Sh0 and Sh1 values using Rock-Eval pyrolysis.

696 The developed methodology of sample preparation, measurement and data modeling allow to reach
697 several valuable parameters relevant for source rocks studies. Its application seems to give satisfactory

results in comparison with already known parameters. The SAXS measurements could be improved notably. By using shorter wavelength (e.g. molybdenum), transmission would be higher, the exposure time lower and the fluorescence eliminated. If this wavelength is tuned finely around the absorption edge of Fe (ASAXS), the scattering contribution of pyrite should be mitigated rendering the pore content more accurate. As mentioned, data acquired with a better statistic would also allow to consider a smaller azimuthal aperture and to better appreciate the moderate signal of nanopores.

Finally, this fine characterization of the porous media could be seen as a first step before the introduction or the removal of various compounds, including hydrocarbons or CO_2, from the pores space. The proposed methodology, based on contrasts, would allow to probe the affinity of a fluid to pores contained in kerogen and would provide information on the pore connectivity.

5. CONCLUSION

This study was performed to better characterize source rocks for transport or mechanical issues. For that, a new methodology based on SAXS/SANS complementarity is developed. The sample preparation, thin blade section cut normal to bedding, allow to compare directly the anisotropic X-ray and neutron patterns. From 2D scattering analysis, an order parameter likely related to the preferential orientation of lamellar minerals is inferred. It represents a valuable parameter that could be used for mechanical or transport properties issues. At large Q values, an additional isotropic scattering contribution, ascribed to nanopores in kerogen, is evidenced and mostly apparent at specific azimuthal angles. For these later, the 1D scattering profiles are modeled by two contributions related to three distinct phases : minerals, kerogen and pores. These two contributions are weighted by prefactors that are different for each radiation. The exploitation of both prefactor, together with the one of the scattering model allow to retrieve valuables parameters such as a kerogen maturity index, number density of nanopores leading to their size distribution and also their associated volume fraction. The

latter being related to the kerogen maximum storage capacity for gaseous species or condensed fluids. Moreover, X-ray pore space SLD gives some indications about the nature of filling fluids.

This methodology is tested on a series of source rocks of increasing maturities. The same set of geometrical parameters allow to fit both X-ray and neutron data proving the selectivity of the model. The kerogen maturity index is in agreement with the Rock-Eval pyrolysis maturity approximation. The nanopore sizes and their associated volume fraction are in the range of, respectively, 0.5-0.7 nm and 0.01-0.04 for mature source rocks. They are likely filled either by light hydrocarbons, or a mixture of heavy hydrocarbons and empty pores. For the overmature one, an additional pore size of 3.5 nm, accounting for a volume fraction of ~ 0.2%, is evidenced. For both population, pores appears empty in full agreement with Rock-Eval pyrolysis measurements.

This new methodology proved to be efficient and open a new way to look quantitatively at nanoporous kerogen phase and its *in-situ* evolution upon treatment such as emptying or filling it with various fluids.

6. ACKNOWLEDGEMENT

The authors are grateful to IFP Energies Nouvelles and PHENIX laboratory for their financial and scientific support. We thank E. Bemer (IFPEN) and W. Sassi (IFPEN) for providing the source rock samples as part of GASH and MGH projects. We also thank M. Detrez for his technical support on PA20 and the Laboratoire Léon Brillouin which provide SANS instrumentation and the financial support for this experiment. We are grateful to P. Hayrault and F. Moreau for their help respectively on HS-GC interpretation and FESEM experiment. All authors contributed to the discussion, the writing and the review of this paper.

7. SUPPORTING INFORMATION

SAXS measurements on different sample thickness (100, 140 and 200 µm) are provided in supplementary data as an illustration for no multiple scattering effects. Then, I(Q) as a function of lamellar minerals content, for X-ray or neutron radiation, and as a function of TOC content (neutron radiation) are provided. For the fitting procedure, data concerning pyrite modelization on SAXS data and nanopores radius sensitivity, are displayed in supporting information. Chromatograms of HS-GC measurements along source rocks lamination (normal or parallel cut to bedding) are also detailed.

8. REFERENCES

1- Kuuskraa V. A.; Stevens S. H. and Moodhe, K. (2013) World Shale Gas and Shale Oil Resource Assessment. EIA/ARI.

2- Godec M.L.; Jonsson H. and Basava-Reddi L. (2013) Potential Global Implications of Gas Production from Shales and Coal for Geological CO2 Storage. In : Energy Procedia, vol. 37, p. 6656–6666. DOI: 10.1016/j.egypro.2013.06.598.

3- IEA (2007). World Energy Outlook 2007: China and India Insights. In : IEA, Paris, ISBN: 978-92-64-02730-5

4- IEA (2019), World Energy Outlook 2019, In : IEA, Paris https://www.iea.org/reports/world-energy-outlook-2019

5- Bennaceur K.; Gielen D.; Kerr T. and Tam C. (2008) CO_2 capture and storage. A key carbon abatement option. In : International Energy Agency : Organisation for Economic Co-operation and Development. Paris (Energy technology analysis). ISBN : 978-92-64-04140-0

6- Zhao J.; Jin Z.; Hu Q.; Jin Z.; Barber T.J.; Zhang Y. and Bleuel M. (2017) Integrating SANS and fluid-invasion methods to characterize pore structure of typical American shale oil reservoirs. In : Nature communications, vol. 7. DOI: 10.1038/s41598-017-15362-0.

7- Radlinski A.P; Mastalerz M.; Hinde A.L; Hainbuchner M.; Rauch H.; Baron M.; Lin J.S.; Fan L. and Thiyagarajan P. (2004) Application of SAXS and SANS in evaluation of porosity, pore size distribution and surface area of coal. In : International Journal of Coal Geology, vol. 59, n° 3-4, p. 245–271. DOI: 10.1016/j.coal.2004.03.002.

8- Gu X.; Cole D. R.; Rother G.; Mildner D.F.R. and Brantley S.L. (2015) Pores in Marcellus Shale: A Neutron Scattering and FIB-SEM study. In : Energy & Fuels, vol. 29, n° 3, p. 1295–1308. DOI: 10.1021/acs.energyfuels.5b00033

9- Ougier-Simonin A.; Renard F.; Boehm C. and Vidal-Gilbert S. (2016) Microfracturing and Microporosity in Shales. In : Earth-Science Reviews, vol. 162, p. 198-226. DOI : 10.1016/j.aerscirev.2016.09.006

10- Sun M.; Yu B.; Hu Q.; Yang R.; Zhang Y.; Li B.; Melnichenko Y.B. and Cheng G. (2018) Pore structure characterization of organic-rich Niutitang shale from China. Small angle neutron scattering (SANS) study. In : International Journal of Coal Geology, vol. 186, p. 115–125. DOI: 10.1016/j.coal.2017.12.006.

11- Craddock P.R.; Bake K.D. and Pomerantz A.E. (2018) Chemical, Molecular, and Microstructural Evolution of Kerogen during Thermal Maturation: Case study from the Woodford Shale of Oklahoma. In : Energy & Fuels, vol. 32, n° 4, p. 4859–4872. DOI: 10.1021/acs.energyfuels.8b00189

12- Backeberg N. R.; Lacoviello F.; Rittner M.; Mitchell T. M.; Jones A.P.; Day R.; Wheller J.; Shearing P.R.; Vermeesch P.and Striolo A. (2017) Quantifying the Anisotropy and Tortuosity of Permeable Pathways in Clay-Rich Mudstones using Models based on X-ray Tomography. In : Scientific Reports, vol. 7. DOI: 10.1038/s41598-017-14810-1.

13- Rouquerol J.; Avnir D.; Fairbridge C.W.; Everett D.H.; Haynes J.H.; Pernicone N.; Ramsay J.D.F.; Sing K.S.W. and Unger K.K. (1994) Recommendations for the Characterization of Porous Solids. International Union of Pure and Applied Chemistry. In : Pure & Applied Chemistry, vol. 66, n° 8, p. 1739–1758.

14- Mastalerz M.; He L.; Melnichenko Y.B. and Rupp J.A. (2012) Porosity of Coal and Shale. Insights from Gas Adsorption and SANS/USANS Techniques. In : Energy & Fuels, vol. 26, n° 8, p. 5109–5120. DOI: 10.1021/ef300735t.

15- Ruppert L.F.; Sakurovs R.; Blach T.P.; He L.; Melnichenko Y.B.; Mildner D.F.R. and Alcantar-Lopez L. (2013) A USANS/SANS Study of the Accessibility of Pores in the Barnett Shale to Methane and Water. In Energy & Fuel, vol. 27, p. 722-779. DOI : 10.1021/ef301859s

16- Tissot B.P. and Welte D.H. (1984) Petroleum Formation and Occurence. Springer-Verlag.

17- Chalmers G.R.L.; Bustin R.M. and Power I.M. (2012) Characterization of gas shale pore systems by porosimetry, pycnometry, surface area, and field emission scanning electron

microscopy/transmission electron microscopy image analyses. Examples from the Barnett, Woodford, Haynesville, Marcellus, and Doig units. In : AAPG Bulletin, vol. 96, n° 6, p. 1099–1119. DOI: 10.1306/10171111052.

18- Melnichenko Y. B.; Radlinski A. P.; Mastalerz M.; Cheng G. and Rupp, J.A. (2009) Characterization of the CO2 fluid adsorption in coal as a function of pressure using neutron scattering techniques (SANS and USANS). In : International Journal of Coal Geology, vol. 77, n° 1-2, p. 69–79. DOI: 10.1016/j.coal.2008.09.017.

19- Pang Y.; Soliman M.Y.; Deng H. and Xie X. (2017) Experimental and analytical investigation of adsorption effects on shale gas transport in organic nanopores. In : Fuel, vol. 199, p. 272-288. DOI: 10.1016/j.fuel.2017.02.072.

20- Bahadur J.; Radlinski A.P.; Melnichenko Y.B.; Mastalerz M. and Schimmelmann A. (2015) Small-Angle and Ultrasmall-Angle Neutron Scattering (SANS/USANS) Study of New Albany Shale. A Treatise on Microporosity. In : Energy & Fuels, vol. 29, n° 2, p. 567–576. DOI: 10.1021/ef502211w.

21- King H.E.; Eberle A.P.R.; Walters C.C.; Kliewer C.E.; Ertas D. and Huynh C. (2015) Pore Architecture and Connectivity in Gas Shale. In : Energy & Fuels, vol. 29, n° 3, p. 1375–1390. DOI: 10.1021/ef502402e.

22- Eberle A.P.R.; King H.E.; Ravikovitch P.I.; Walters C.C.; Rother G. and Wesolowski, D.J. (2016) Direct Measure of the Dense Methane Phase in Gas Shale Organic Porosity by Neutron Scattering. In : Energy & Fuels, vol. 30, n° 11, p. 9022–9027. DOI: 10.1021/acs.energyfuels.6b01548.

23- Sun M.; Yu B.; Hu Q.; Zhang Y.; Li B.; Yang R.; Melnichenko Y.B. and Cheng G. (2017) Pore characteristics of Longmaxi shale gas reservoir in the Northwest of Guizhou, China. Investigations using small-angle neutron scattering (SANS), helium pycnometry, and gas sorption isotherm. In : International Journal of Coal Geology, vol. 171, p. 61–68. DOI: 10.1016/j.coal.2016.12.004.

24- Yang R.; He S.; Hu Q.; Sun M.; Hu D. and Yi J. (2017) Applying SANS technique to characterize nano-scale pore structure of Longmaxi shale, Sichuan Basin (China). In : Fuel, vol. 197, p. 91–99. DOI: 10.1016/j.fuel.2017.02.005.

25- Zhang R.; Liu S. and Wang Y. (2017) Fractal evolution under in situ pressure and sorption conditions for coal and shale. In : Scientific reports, vol. 7, n° 1, p. 8971. DOI: 10.1038/s41598-017-09324-9.

26- Bodhisatwa H.; Suryendu D. and Sumit K. (2017) TOC calculation of organic matter rich sediments using Rock-Eval pyrolysis: Critical consideration and insights. In : International Journal of Coal Geology, vol. 169, p. 106–115.

27- Clarkson C. R.; Freeman M.; He L.; Agamalian, M.; Melnichenko, Y. B.; Mastalerz, M.; Bustin R.M.; Radlinski A.P. and Blach T.P. (2012) Characterization of tight gas reservoir pore structure using USANS/SANS and gas adsorption analysis. In : Fuel, vol. 95, p. 371–385. DOI: 10.1016/j.fuel.2011.12.010.

28- Clarkson C.R.; Solano N.; Bustin R.M.; Bustin A.M.M.; Chalmers G.R.L.; He, L.; Melnichenko Y.B.; Radlinski A.P. and Blach T.P. (2013) Pore structure characterization of North American shale gas reservoirs using USANS/SANS, gas adsorption, and mercury intrusion. In : Fuel, vol. 103, p. 606–616. DOI: 10.1016/j.fuel.2012.06.119.

29- Han H.; Cao Y.; Chen S.; Lu J.; Huang C.; Zhu H.; Zhan P. and Gao Y. (2016) Influence of particle size on gas-adsorption experiments of shales. An example from a Longmaxi Shale sample from the Sichuan Basin, China. In : Fuel, vol. 186, p. 750–757. DOI: 10.1016/j.fuel.2016.09.018.

30- Li P.; Jiang Z.; Zheng M.; Bi H. and Chen L. (2016) Estimation of shale gas adsorption capacity of the Longmaxi Formation in the Upper Yangtze Platform, China. In : Journal of Natural Gas Science and Engineering, vol. 34, p. 1034–1043. DOI: 10.1016/j.jngse.2016.07.052.

31- Romero-Sarmiento M.F.; Pillot D.; Letort G.; Lamoureux-Var V.; Beaumont V.; Huc A.Y. and Garcia B. (2016) New Rock-Eval Method for Characterization of Unconventional Shale Resource Systems. In : Oil & Gas Science and Technology – Revue d'IFP Energies nouvelles, vol. 71, n° 3, p. 37. DOI: 10.2516/ogst/2015007.

32- Wang P.; Jiang Z.; Yin L.; Chen L.; Li Z.; Zhang C.; Li T. and Huang P. (2017) Lithofacies classification and its effect on pore structure of the Cambrian marine shale in the Upper Yangtze Platform, South China. Evidence from FE-SEM and gas adsorption analysis. In : Journal of Petroleum Science and Engineering, vol. 156, p. 307–321. DOI: 10.1016/j.petrol.2017.06.011.

33- Melnichenko Y.B. (2016) Small-Angle Scattering from Confined and Interfacial Fluids. Cham : Springer International Publishing.

34- Anovitz L M.; Cole D. R. (2015) Characterization and Analysis of Porosity and Pore Structures. In : Reviews in Mineralogy and Geochemistry, vol. 80, n° 1, p. 61–164. DOI: 10.2138/rmg.2015.80.04.

35- Bahadur J.; Melnichenko Y. B.; Mastalerz M.; Furmann A. and Clarkson C.R. (2014) Hierarchical Pore Morphology of Cretaceous Shale. A Small-Angle Neutron Scattering and

Ultrasmall-Angle Neutron Scattering Study. In : Energy & Fuels, vol. 28, n° 10, p. 6336–6344. DOI: 10.1021/ef501832k.

36- Chalmers G.R.L. and Bustin R.M. (2015) Porosity and Pore Size Distribution of Deeply-Buried Fine-Grained Rocks: Influence of Diagenetic and Metamorphic Processes on Shale Reservoir Quality and Exploration. In : Journal of Unconventional Oil and Gas Resources, vol. 12, p. 134–142. DOI: 10.1016/j.juogr.2015.09.005

37- Clarkson C.R.; Haghshenas B.; Ghanizadeh A.; Qanbari F.; Williams-Kovacs J.D.; Riazi, N.; Debuhr C. and Deglint H.J. (2016) Nanopores to megafractures. Current challenges and methods for shale gas reservoir and hydraulic fracture characterization. In : Journal of Natural Gas Science and Engineering, vol. 31, p. 612–657. DOI: 10.1016/j.jngse.2016.01.041.

38- Liu S.; Zhang R.; Karpyn Z.T.; Yoon H. and Dewers T. (2019) Investigation of accessible pore structure evolution under pressurization and adsorption for coal and shale using small-angle neutron scattering. In : Energy & Fuels. DOI: 10.1021/acs.energyfuels.8b03672.

39- Radlinski A.P.; Boreham C.J.; Lindner P.; Randl O.; Wignall G.D.; Hinde A. and Hope J.M. (2000) Small Angle Neutron Scattering Signature of Oil Generation in Artificially and Naturally Matured Hydrocarbon Source Rocks. In : Organic Geochemistry, vol. 31, p. 1-14. DOI: 10.1016/S0146-6380(99)00128-X

40- Kang S.M.; Fathi E.; Ambrose R.J.; Akkutlu I.Y. and Sigal R.F. (2011) Carbon Dioxide Storage Capacity of Organic-Rich Shales. In : SPE Journal, vol. 16, p. 842-855. DOI: 10.2118/134583-PA.

41- Bodhisatwa H.; Wood D.A.; Vishal V. and Singh A.K. (2018) Pore Characteristics of Distinct Thermally Mature Shales : Influence of Particle Size on Low-Pressure CO_2 and N_2 Adsorption. In : Energy and Fuels, vol. 32, p. 8175-8186. DOI: 10.1021/acs.energyfuels.8b01439.

42- Davudov D.; Moghanloo R.G. and Lan Y. (2018) Evaluation of Accessible Porosity Using Mercury Injection Capillary Pressure Data in Shale Samples. In : Energy and Fuels, vol. 32, p. 4682-4694. DOI: 10.1021/acs.energyfuels.7b03930.

43- Habina I.; Radzik N.; Topór T. and Krzyżak A.T. (2017) Insight Into Oil and Gas-Shales Compounds Signatures in Low Field 1 H NMR and its Application in Porosity Evaluation. In : Microporous and Mesoporous Materials, vol. 252, p. 37–49. DOI: 10.1016/j.micromeso.2017.05.054.

44- Shaoqing T.; Yanhui D.; Qian Z.; Derek E.; Shimin L. (2017) Quantitative Analysis of Nanopore Structural Characteristics of Lower Paleozoic Shale, Chongqing (Southwestern China): Combining FIB-SEM and NMR Cryoporometry. In : Energy and Fuels, vol. 31, p. 13317-13328. DOI: 10.1021/acs.energyfuels.7b02391

45- Xinhe S.; Xiongqi P.; Hui L. and Xue Z. (2017) Fractal Analysis of Pore Network in Tight Gas Sandstones Using NMR Method: A Case Study from the Ordos Basin, China. In : Energy and Fuels, vol. 10, n° 31. DOI: 10.1021/acs.energyfuels.7b01007.

46- Fleury M.; Fabre R. and Webber J.B.W. (2015) Comparison of Pore Size Distribution by NMR Relaxation and Nmr Cryoporometry in Shales. In : Society of Core Analysis.

47- Korb J.P.; Nicot B.; Louis-Joseph A.; Bubici S. and Ferrante G.(2014) Dynamics and Wettability of Oil and Water in Oil Shales. In : The Journal of Physical Chemistry C, vol. 118, n° 40, p. 23212–23218. DOI: 10.1021/jp508659e.

48- Radlinski A. P.; Hinde A. L.; Rauch H.; Hainbuchner M.; Baron M.; Mastalerz M.; Ioannidis M. and Thiyagarajan P. (2005) The microstructure of rocks and small-angle and ultra-small-angle neutron scattering: the coming of age of a new technique. In : Geophysical Research Abstracts, vol. 7.

49- Lee S.; Fischer T.B.; Stokes M.R.; Klingler R.J.; Ilavsky J.; McCarty D.K.; Wigand M.O.; Derkowski A. and Winans R.E., (2014) Dehydration Effect on Pore Size, Porosity, and Fractal Parameters of Shale Rocks: USAXS Study. In : Energy and Fuels, vol. 28, p. 6772-6779. DOI: 10.1021/ef501427d.

50- Leu L.; Georgiadis A.; Blunt M.J.; Busch A.; Bertier P.; Schweinar K.; Liebi M.; Menzel A. and Ott H. (2016) Multiscale Description of Shale Pore Systems by Scanning SAXS and WAXS Microscopy. In : Energy and Fuels, vol. 30, p.10282-10297. DOI: 10.1021/acs.energyfuels.6b02256.

51- Hall P.L.; Mildner D.F.R. and Borst R.L. (1986) Small-angle scattering studies of the pore spaces of shaly rocks. In : Journal of Geophysical Research, vol. 91, n° B2, p. 2183. DOI: 10.1029/JB091iB02p02183.

52- Pillot D.; Letort G.; Romero-Sarmiento M.F.; Lamoureux-Var V.; Beaumont V. and Garcia B. (2014) Method of Assessing at Least one Petroleum Characteristic of a Rock Sample. Patent 14/55.009.

53- Chen S.; Han Y.; Fu C.; Zhang H.; Zhu Y. and Zuo Z. (2016) Micro and nano-size pores of clay minerals in shale reservoirs. Implication for the accumulation of shale gas. In : Sedimentary Geology, vol. 342, p. 180–190. DOI: 10.1016/j.sedgeo.2016.06.022.

54- Espitalié J.; Deroo G. and Marquis F. (1986) La Pyrolyse Rock-Eval et ses Applications : Troisième Partie. In : Revue de l'Institut Français du Pétrole, Vol. 41, p. 73-89. DOI : 10.2516/osgt :1986003.

55- Liao L.; Wang Y.; Chen C.; Shi S. and Deng R. (2018) Kinetic study of marine and lacustrine shale grains using Rock-Eval pyrolysis. Implications to hydrocarbon generation, retention and expulsion. In : Marine and Petroleum Geology, vol. 89, p. 164–173. DOI: 10.1016/j.marpetgeo.2017.01.009.

56- Ghanizadeh A.; Bhowmik S.; Haeri-Ardakani O.; Sanei H. and Clarkson C.R. (2015)a A Comparison of Shale Permeability Coefficients Derived using Multiple Non-Steady-State Measurement Techniques: Examples frome the Devernay Formation, Alberta (Canada). In : Fuel, vol. 140, p. 371-387. DOI:10.1016/j.fuel.2014.09.073.

57- Ghanizadeh A.; Clarkson C.R.; Aquino S.; Haeri-Ardakani O. and Sanei H. (2015)b Petrophysical and Geomechanical Characteristics of Candaian Tight Oil and Liquid-Rich Gas Reservoirs: I. Pore Network and Permeability Characterization. In : Fuel, vol. 153, p. 664-681. DOI: 10.1016/j.fuel.2015.03.020.

58- Bernard S.; Horsfield B.; Schulz H.M.; Schreiber A.; Wirth R.; Anh Vu T.T.; Perssen F.; Könitzer S.; Volk H.; Sherwood N. and Fuentes D. (2010) Multi-Scale Detection of Organic and Inorganic Signatures Provides Insights into Gas Shale Properties and Evolution. In : Chemie der Erde, vol. 70, p. 119-133. DOI: 10.1016/j.chemer.2010.05.005.

59- Bernard S.; Wirth R.; Schreiber A.; Schulz H.M. and Horsfield B. (2012) Formation of Nanoporous Pyrobitumen Residues During Maturation of the Barnett Shale (Fort Worth Basin). In : Internation Journal of Coal Geology, vol. 103, p. 3-11. DOI : 10.1016/j.coal.2012.04.010.

60- Jayne R.S.; Wu H. and Pollyea R.M. (2019) Geologic CO_2 Sequestration and Permeability Uncertainty in a Highly Heterogeneous Reservoir. In : International Journal of Greenhouse Gas Control, vol. 83, p. 128-139. DOI: 10.1016/j.ijggc.02.001.

61- Medina C.R.; Mastalerz M. and Rupp J.A. (2018) Pore System Characterization of Cambrian-Ordovician Carbonates Using a New Mercury Porosimetry-Based Petrofacies Classification System: Application to Carbon Sequestration Reservoirs. In : Greenhouse Gases Science and Technology, vol. 8, p. 932-953. DOI : 10.1002/ghg

62- Rietveld H.M. A Profile Refinement Method for Nuclear and Magnetic Structure. Journal of Applied Crystallography, 1969, vol. 2, p. 65-71. DOI: 10.1107/S0021889869006558

63- Loucks R.G. and Ruppel S.C. (2007) Mississippian Barnett Shale. Lithofacies and depositional setting of a deep-water shale-gas succession in the Fort Worth Basin, Texas. In : AAPG Bulletin, vol. 91, n° 4, p. 579–601. DOI: 10.1306/11020606059.

64- Davidson P.; Petermann D. and Levelut A.M. (1995) The Measurement of Nematic Order Parameter by X-ray Scattering Reconsidered. In : Journal de Physique II, vol. 5, p. 113-131. DOI: 10.1051/jp2:1995117.

65- Paineau E.; Antonova K.; Baravian C.; Bihannic I.; Davidson P.; Dozov I.; Impéror-Clerc M.; Levitz P.; Madsen A.; Meneau F. and Michot L.J. (2009) Liquid-Crystalline Nematic Phase in Aqueous Suspensions of a Disk-Shaped Natural Beidellite Clay. In : Journal of Physical Chemistry B, vol. 113, p. 15858-15869. DOI: 10.1021/jp908326y

66- Paineau E.; Krapf M.E.M.; Amara M.S.; Matskova N.V.; Dozov I.; Rouzière S.; Thill A.; Launois P. and Davidson P. (2016) A Liquid-Crystallin Hexagonal Columnar Phase in Highly-Dilute

Suspensions of Imogolite Nanotubes. In : Nature Communications, vol. 7. DOI : 10.1038/ncomms10271

67- Suzzoni A.; Barré L.; Kohler E.; Levitz P.; Michot L.J. and M'Hamdi J. (2018) Interactions between Kaolinte Clay and AOT. In : Colloids and Surfaces A: Physicochemical and Engineering Aspects, vol 556, p. 309-315. DOI: 10.1016/j.colsurfa.2018.07.049

68- Maier V.W. and Saupe A. (1959) Theorie der Nematischen Kristallinflüssigen Phase. Teil I. In : Z. Naturforschg, vol. 14a, p. 882-889.

69- Maier V.W. and Saupe A. (1960) Eine Einfache Molekular-Statistische Theorie der Nematischen Kristallinflüssigen Phase. Teil II. In : Z. Naturforschg, vol. 15a, p. 287-292.

70- Ilgen A.G.; Heath J.E.; Akkutlu I.Y.; Bryndzia L.T.; Cole D.R.; Kharaka Y.K.; Kneafsey T.J.; Miliken K.L.; Pyrak-Nolte L.J. and Suarez-Rivera R. (2017) Shales at all scales. Exploring coupled processes in mudrocks. In : Earth-Science Reviews, vol. 166, p. 132–152. DOI: 10.1016/j.earscirev.2016.12.013.

71- Thomas J.J.; Valenza J.J.; Craddock P.R.; Bake K.D. and Pomerantz A.E. (2014) The neutron scattering length density of Kerogen and coal as determined by CH3OH/CD3OH exchange. In : Fuel, vol. 117, p. 801–808. DOI: 10.1016/j.fuel.2013.09.075.

72- Espinat D. (1990) Applications des techniques de diffusion de la lumière, des rayons X et des neutrons à l'étude des systèmes colloïdaux. ISBN : 2-7108-0617-7

73- Arthur M.A. and Cole D.R. (2014) Unconventional Hydrocarbon Resources. Prospects and Problems. In : Elements, vol. 10, p. 257-264. DOI: 10.2113/gselements.10.4.257

74- Bazilevskaya E.; Rother G.; Mildner D.F.R.; Pavich M.; Cole D. and Bhatt M.P. (2015) How Oxidation and Dissolution in Diabase and Granite Control Porosity during Weathering. In : Soil Science Society of American Journal, vol. 79, p. 55. DOI: 10.2136/sssaj2014.04.0135

75- Bale H.D. and Schmidt P.W., (1984) Small-Angle X-Ray-Scattering Investigation of Submicroscopic Porosity with Fractal Properties. In : Physical Review Letters, vol. 53. DOI: 10.1103/PhysRevLett.53.596.

76- Broseta, D.; Barré, L.; Vizika, O.; Shahidzadeh, N.; Guilbaud, J. P.; Lyonnard, S. (2001) Capillary Condensation in a Fractal Porous Medium. In : Physical Review Letters, vol. 86, p. 5313-5316. DOI: 10.1103/PhysRevLett.86.5313

77- Radlinski A.P. (2006) Small-Angle Neutron Scattering and the Microstructure of Rocks. In Reviews in Mineralogy & Geochemistry, vol. 63, p. 363-397. DOI : 10.2138/rmg.2006.63.14

78- Schmidt P.W. (1982) Interpretation of Small-Angle Scattering Curves Proportional to a Negative Power of the Scattering Vector. In : Journal of Applied Crystallography, vol. 15, p. 567-569. DOI: 10.1107/S002188988201259X.

79- Bahadur J.; Ruppert L.F.; Pipich V.; Sakurovs R. and Melnichenko Y.B. (2018) Porosity of the Marcellus Shale. A contrast matching small-angle neutron scattering study. In : International Journal of Coal Geology, vol. 188, p. 156–164. DOI: 10.1016/j.coal.2018.02.002.

80- Blach T.; Radlinski A.P.; Edwards D.S.; Boreham C.J.; Rehm C.; Campo L. and Gilbert E.P. (2018) Fingerprint of hydrocarbon generation in the southern Georgina Basin, Australia, revealed by small angle neutron scattering. In : International Journal of Coal Geology, vol. 186, p. 135–144. DOI: 10.1016/j.coal.2017.10.013.

81- Bressler I.; Kohlbrecher J. and Thünemann A. F. (2015) SASfit: a Tool for Small-Angle Scattering Data Analysis using a Library of Analytical Expressions. In : Journal of Applied Crystallography, vol. 48, p. 1587-1598. DOI: 10.1107/S1600576715016544.

82- Liu S. and Zhang R. (2020) Anisotropic Pore Structure of Shale and Gas Injection-Induced Nanopore Alteration : A Small-Angle Neutron Scattering Study. In : Internation Journal of Coal Geology, vol. 219. DOI: 10.1016/j.coal.2020.103384.

83- Kwon O.; Kronenberg A.K.; Gangi A.F.; Johnson B. and Herbert B.E. (2004) Permeability of Illite-Bearing shale : 1. Anisotropy and Effects of Clay Content and Loading. In : Journal of Geophysical Research, vol. 109, B10205. DOI: 10.1029/2004JB003052.

84- Dabat T.; Porion P.; Hubert F.; Paineau E.; Dazas B.; Grégoire B.; Tertre E.; Delville A. and Ferrage E. (2020) Influence of Preferred Orientation of Clay Particles on the Diffusion of Water in Kaolinite Porous Media at Constant Porosity. In : Applied Clay Science, vol. 184. DOI: 10.1016/j.clay.2019.105354

85- Sui J. (2019) Stratification in the Dynamics of Sedimenting Colloidal Platelet-Sphere Mixture. In : Soft Matter, vol. 23., p. 4714-4722 DOI: 10.1039/C9SM00485H

86- Forny-Le-Follotec A.; Glatter O.; Pezron I.; Barré L.; Noik C.; Dalmazzone C. and Metlas-Komunjer L. (2012) Characterization of Micelles of Small Triblock Copolymer by Small-Angle Scattering. In : Macromolecules, vol. 45, p. 2874-2881. DOI: 10.1021/ma201610n

87- Eyssautier J.; Levitz P.; Espinat D.; Jestin J.; Gummel J.; Grillo I. and Barré L. (2011) Insight into Asphaltene Nanoaggragate Structure Inferred by Small Angle Neutron and X-ray Scattering. In : The Journal of Physical Chemistry B, vol. 115, p. 6827-6837. DOI: 10.1021/jp111468d

88- Bousige C.; Matei Ghimbeu C.; Vix-Guteri C.; Pomerantz A.E.; Suleimenova A.; Vaughan G.; Garbarino G.; Feygenson M.; Wildgruber C.; Ulm F.J.; Pellenq R.J.M. and Coasne B. (2016) Realistic Molecular Model of Kerogen's Nanostructure. In : Nature materials. DOI: 10.1038/NMAT4541